Hubble space telescope near-infrared snapshot survey of 3CR radio source counterparts. II. An atlas and inventory of the host galaxies, mergers, and companions

Article (Published Version)

The Astrophysical Journal Supplement Series, 177:148–173, 2008 July

HUBBLE SPACE TELESCOPE NEAR-INFRARED SNAPSHOT SURVEY OF 3CR RADIO SOURCE COUNTERPARTS. II. AN ATLAS AND INVENTORY OF THE HOST GALAXIES, MERGERS, AND COMPANIONS[1]

David J. E. Floyd,[2] David Axon,[3] Stefi Baum,[3] Alessandro Capetti,[4] Marco Chiaberge,[2]
Duccio Macchetto,[2] Juan Madrid,[2] George Miley,[5] Christopher P. O'Dea,[3]
Eric Perlman,[6] Alice Quillen,[7] William Sparks,[2] and Grant Tremblay[2]
Received 2007 August 7; accepted 2007 December 4

ABSTRACT

We present the second part of an *H*-band (1.6 μm) "atlas" of $z < 0.3$ 3CR radio galaxies, using the *Hubble Space Telescope* Near Infrared Camera and Multi-Object Spectrometer (*HST* NICMOS2). We present new imaging for 21 recently acquired sources and host galaxy modeling for the full sample of 101 (including 11 archival)—an 87% completion rate. Two different modeling techniques are applied, following those adopted by the galaxy morphology and the quasar host galaxy communities. Results are compared and found to be in excellent agreement, although the former breaks down in the case of sources with strong active galactic nuclei (AGNs). Companion sources are tabulated, and the presence of mergers, tidal features, dust disks, and jets are cataloged. The tables form a catalog for those interested in the structural and morphological dust-free host galaxy properties of the 3CR sample, and for comparison with morphological studies of quiescent galaxies and quasar host galaxies. Host galaxy masses are estimated and found to typically lie at around $2 \times 10^{11}\ M_{\odot}$. In general, the population is found to be consistent with the local population of quiescent elliptical galaxies, but with a longer tail to low Sérsic index, mainly consisting of low-redshift ($z < 0.1$) and low-radio-power (FR I) sources. A few unusually disky FR II host galaxies are picked out for further discussion. Nearby external sources are identified in the majority of our images, many of which we argue are likely to be companion galaxies or merger remnants. The reduced NICMOS data are now publicly available from our Web site.

Subject headings: galaxies: active — galaxies: fundamental parameters

Online material: machine-readable tables

1. INTRODUCTION

Extragalactic radio sources have long posed an enigma to our understanding of the universe. While they can occupy some of the most gravitationally dominant galaxies in clusters, their bolometric luminosity is dominated not by the starlight from their galactic hosts but by the (often physically much vaster) regions of low-density radio-emitting material that have an origin in a tiny region of space at their very core. We now understand that the physics of these objects is related to the supermassive ($\gtrsim 10^8\ M_{\odot}$) black holes residing at their cores and the fueling of these black holes by accretion of gas and dust. However, it is still unclear why so many apparently optically similar galaxies exist in the universe with no sign of radio activity. What makes one black hole radio active, and another not? The concept of a black-hole duty-cycle (Richstone et al. 1998) as the fraction of black holes that are active at any time is a useful statistical characterization, but we still do not understand what physically drives it. It is known that, broadly, the comoving number density of black holes evolves along with the cosmic star formation rate, and this can be seen as a correlation between the evolution of the black hole duty cycle and that of the cosmic star formation rate (Wang et al. 2006). Mergers have long been regarded as a strong candidate for triggering AGN activity, providing a mechanism for the delivering the necessary (gas and dust) fuel to the central regions of a galaxy and the black hole therein (Kauffmann & Haehnelt 2000; Di Matteo et al. 2005). Studies have shown the presence of nuclear dust disks in the cores of many radio galaxies (Sadler & Gerhard 1985; van Dokkum & Franx 1995), but similar numbers are also found in quiescent galaxies (Veron-Cetty & Veron 1988). Early studies of quasars showed morphological disturbances or tidal features to be present in many of the host galaxies (e.g., Smith et al. 1986; Hutchings & Neff 1992; Bahcall et al. 1997), but more recent (and better selected) samples have shown that the proportion exhibiting major tidal features is indistinguishable from that in the quiescent elliptical galaxy population (Dunlop et al. 2003; Floyd et al. 2004). Thus, today it remains unclear whether there are any optical-IR properties of radio galaxies that distinguish them as a class from the putative parent population of quiescent elliptical galaxies, rather than simply being inherited from them.

In recent years, much attention has been drawn to the correlation seen locally between bulge and black hole mass in normal quiescent elliptical galaxies (e.g., Gebhardt et al. 2000; Merritt & Ferrarese 2001). AGNs provide two obvious possible feedback mechanisms under which such a relation might arise, through radiation pressure and through the action of radio jets emanating from the central engine. Theoretical developments and recent numerical studies using semianalytic models (e.g., Croton et al.

[1] Based on observations with the NASA / ESA *Hubble Space Telescope*, obtained at the Space Telescope Science Institute, which is operated by the Association of Universities for Research in Astronomy, Inc. (AURA), under NASA contract NAS5-26555.

[2] Space Telescope Science Institute, 3700 San Martin Drive, Baltimore, MD 21218; dfloyd@lco.cl.

[3] Department of Physics, Rochester Institute of Technology, 85 Lomb Memorial Drive, Rochester, NY 14623.

[4] INAF–Osservatorio Astronomico di Torino, Strada Osservatorio 20, Pino Torinese I-10025, Italy.

[5] Leiden Observatory, P.O. Box 9513, NL-2300 RA Leiden, The Netherlands.

[6] Florida Institute of Technology, Physics, and Space Sciences Department, 150 West University Boulevard, Melbourne, FL 32901.

[7] Department of Physics and Astronomy, University of Rochester, Bausch, and Lomb Hall, P.O. Box 270171, 600 Wilson Boulevard, Rochester, NY 14627.

2006) to explore the evolution of galaxies have shown that AGN feedback can in principal enforce such a correlation by shutting off star formation and ejecting gas and dust from the most massive galaxies. The same models offer a natural solution to the problems of overproduction of very massive galaxy halos, and simultaneously can explain the "red sequence" of galaxies (e.g., Cattaneo et al. 2006; Di Matteo et al. 2005; Springel et al. 2005). Best et al. (2006) showed that the radio-loud phase of AGN activity is able to suppress the cooling of the host galaxy halo gas sufficiently that the radio source can control the rate of growth of the elliptical galaxy.

It is important to investigate whether any statistical differences can be detected between samples of radio-loud AGNs and samples of quiescent galaxies or radio-quiet AGNs. One difficulty is the way in which active and quiescent galaxies have traditionally been studied is rather different. The most detailed morphological studies of large samples of quiescent galaxies are not conducted in the same way as studies of radio galaxies, or the host galaxies of quasars and other AGNs. To investigate the causes of AGN activity and radio-loudness we need large samples of objects in which *both* AGNs and environment can be explored at multiple wavelengths. The 3C makes an ideal such sample for studying the effect of radio-loud AGN activity on host galaxy environment, and vice versa. Here we focus on the 3CR, a well-defined subsample of the most powerful northern hemisphere radio galaxies (Bennett 1962; Spinrad et al. 1985). We aim to provide a complete inventory of the properties of the low-redshift ($z < 0.3$) 3CR, including physical characterization of the host galaxies free of dust to determine the underlying galaxy structure and dominant stellar mass; the presence of companions, mergers, dust disks, and jets; and the clear detection of any unresolved optical-IR nuclear sources. This will enable us to explore whether anything distinguishes them from normal quiescent galaxies and continue the ongoing study into the question of what makes radio galaxies "radio loud."

1.1. *The 3CR Snapshot Program*

In *HST* cycle 13 (2004–2005) we embarked on a Near-Infrared Camera and Multi-Object Spectrometer (NICMOS) *H*-band snapshot imaging campaign of $z < 0.3$ 3CR sources (Madrid et al. 2006, hereafter Paper I). The infrared is an important realm for our growing understanding of the relationship between AGNs and galaxies, enabling us to study the underlying host galaxies free from the distorting effects of dust. The SNAP program is now complete, having continued through cycle 14 (2005–2006) at reduced priority. Since publication of Paper I (which presented images for the first 69 targets, observed during cycle 13) an additional 22 sources have been successfully observed, and images for these new targets are presented here. Finally, archival data for an additional 11 objects previously observed with NICMOS2 in F160W were obtained from the Multimission Archive at Space Telescope (MAST).[8]

In this paper we seek to characterize the local 3CR host galaxy population in such a way that they can easily be compared to similarly large samples of quiescent galaxies, mergers, radio-loud and radio-quiet quasar host galaxies, and brightest cluster members. We present modeling of all the data using elliptical isophote (one-dimensional radial profile fitting) and two-component two-dimensional galaxy-modeling techniques. We present the sample, observations, and data reduction in § 2. We discuss the one-dimensional (1D) and two-dimensional (2D) modeling of the NIR (*H*-band) host galaxies in § 3. In § 4 we present notes on, and images of, the newly observed and archival targets that were not presented in Paper I. Basic host galaxy properties are presented, and the modeling techniques compared in § 5. In § 6 we present a census of the companion sources and merger environments of the sample. Section 7 presents a general discussion of the sample and study and suggestions for the future. Section 8 concludes with a summary of our main findings. Detailed comparison of the sample with control samples of ellipticals, quasars, and mergers is left to a companion paper (D. J. E. Floyd et al. 2008, in preparation). We have made all of our reduced data publicly available on the Internet.[9]

TABLE 1
Observing Log

Source	α (J2000.0)	δ (J2000.0)	z	λ	Obs. Date
3C 15	00 37 04.1	−01 09 08	0.073	−64	2006 Jun 24
3C 17	00 38 20.5	−02 07 40	0.219	−65	2006 Jul 02
3C 33	01 08 53.3	+13 20 25	0.059	−49	2006 Jun 29
3C 98	03 58 54.4	+10 26 03	0.030	−31	2005 Nov 25
3C 132	04 56 43.0	+22 49 22	0.214	−13	2005 Nov 24
3C 153	06 09 32.5	+48 04 15	0.277	13	2005 Nov 25
3C 166	06 45 24.1	+21 21 51	0.245	8	2005 Nov 04
3C 234	10 01 49.5	+28 47 09	0.185	53	2005 Nov 03
3C 258	11 24 43.5	+19 19 12	0.165	69	2006 Jan 25
3C 284	13 11 04.7	+27 28 08	0.239	86	2006 Mar 04
3C 296	14 16 52.9	+10 48 26	0.025	64	2006 Apr 21
3C 300	14 23 01.0	+19 35 17	0.270	68	2006 Mar 04
3C 323.1	15 47 43.5	+20 52 17	0.264	49	2006 Apr 21
3C 326	15 52 09.1	+20 05 24	0.090	48	2006 Apr 21
3C 332	14 23 01.0	+19 35 17	0.270	45	2006 Jan 12
3C 357	17 28 18.5	+31 46 14	0.166	31	2006 Mar 25
3C 403.1	19 52 30.4	−01 17 20	0.055	−14	2006 Jun 23
3C 410	20 20 06.5	+29 42 14	0.248	−4	2006 Jun 30
3C 424	20 48 12.1	+07 01 18	0.127	−22	2006 Jun 22
3C 442	22 14 46.9	+13 50 27	0.026	−34	2006 Jun 27
3C 459	23 16 35.1	+04 05 19	0.219	−51	2006 Jun 24

Notes.—Observation dates and positions of the 21 newly observed sources in the sample. We present the source name, J2000.0 equatorial coordinates, redshift, Galactic latitude, and observing date. Two other targets, 3C 18 and 3C 63, were observed as part of the program but were missed by the NIC2 chip. The units of right ascention are hours, minutes, and seconds, and the units of declination are degrees, arcminutes, and arcseconds.

2. SAMPLE AND DATA REDUCTION

The majority of the data that we use in this paper were taken during the *HST* Snapshot Program SNAP-10173 (PI: W. Sparks). The near-infrared images, fluxes, and notes for the first 69 of our targets were presented in Paper I. In this paper we present the imaging for 21 additional targets that were unobserved at the time of Paper I's publication. An observing log for these newly observed sources is presented in Table 1. In addition, we analyze archival NICMOS2 F160W data that exist for a further 11 objects (see Table 2). Note that NIC1 and NIC3 lack the field of view and the resolution (respectively) for this morphological study, so observations of 3CR sources on those two chips in the archive have been omitted from study here. Finally, the NIC2 observations of 3C 273 were unsuitable for the present study as they provide only 30 s of on-galaxy integration, with the bulk of the observing time being dedicated to the famous jet. Altogether this selection produces a near-complete sample of 101 powerful ($L_{5\,\mathrm{GHz}} < 10^{-24}$ W Hz^{-1} sr^{-1}) northern hemisphere radio sources at $z < 0.3$ observed in a single infrared band. Radio luminosities

[8] See http://archive.stsci.edu/.

[9] See http://archive.stsci.edu/prepds/3cr/.

TABLE 2
ARCHIVAL OBJECTS: OBSERVATION DATES

Source	Alt. Names	α (J2000.0)	δ (J2000.0)	z	λ	Obs. Date	PROPOSID	Reference
3C 71	M77, NGC 1068	02 42 40.7	−00 00 48	0.003793	−52	1998 Feb 21	7215	1
3C 84	Per A, NGC 1275, A0426	03 19 48.1	+41 30 42	0.017559	−13	1998 Mar 16	7330	2
3C 264	NGC 3862, A1367	11 45 05.0	+19 36 23	0.021718	73	1998 May 12	7862	3
3C 270	NGC 4261	12 19 23.2	+05 49 31	0.007465	67	1998 Apr 23	7868	4
3C 272.1	M84, NGC 4374	12 25 03.7	+12 53 13	0.003536	74	1998 Jul 13	7868	5
3C 274	M87, NGC 4486	12 30 49.4	+12 23 28	0.004360	75	1997 Nov 20	7171	6
3C 293	UGC 08782	13 52 17.8	+31 26 46	0.045034	76	1998 Aug 19	7853	7
3C 305	UGC 09553, IC 1065	14 49 21.6	+63 16 14	0.041639	49	1998 Jul 19	7853	8
3C 317	UGC 09799, A2052	15 16 44.5	+07 01 17	0.034457	50	1998 Aug 26	7886	4
3C 338	NGC 6166, A2199	16 28 38.5	+39 33 06	0.030354	44	1997 Dec 18	7453	9
3C 405	Cyg A	19 59 28.3	+40 44 02	0.056075	6	1997 Dec 16	7258	10

NOTES.—Observation dates and positions of the 11 archival objects in the sample. All observations are on NIC2 through the F160W filter. We list *HST* proposal IDs and references for the original publication of the data. 3C 273 also has deep NICMOS F160W imaging of its jet, but is excluded from this paper as the on-galaxy integration time is too short for an accurate characterization of the host galaxy. Units of right ascention are hours, minutes, and seconds, and units of declination are degrees, arcminutes, and arcseconds.

REFERENCES.—(1) Thompson & Corbin 1999; (2) Martini et al. 2003; (3) Capetti et al. 2000b; (4) Quillen et al. 2000; (5) Bower et al. 2000; (6) Corbin et al. 2002; (7) Floyd et al. 2006a; (8) Jackson et al. 2003; (9) Jensen et al. 2001; (10) Tadhunter et al. 1999.

(at 178 MHz) for the full sample are plotted in Figure 1. Other basic sample data are presented in Table 3. Notes on and images of the newly observed and archival targets are presented in § 4. See Paper I for images of and notes on the other 69 sources.

We have rereduced all of the original data presented in Paper I, along with the new observations presented here, as described below. This new technique conserves the sky background throughout for all sources (allowing for better determination of the image statistics, which is essential for accurate morphological characterization) and maintains the original pixel scale of 0.075″, which is near critically resolved, and perfectly adequate for large-scale morphological studies such as this. On a large sample, the modeling of dithered images with double the spatial resolution results in an impractical increase in the computational time due to the convolution of each image with a point-spread function.

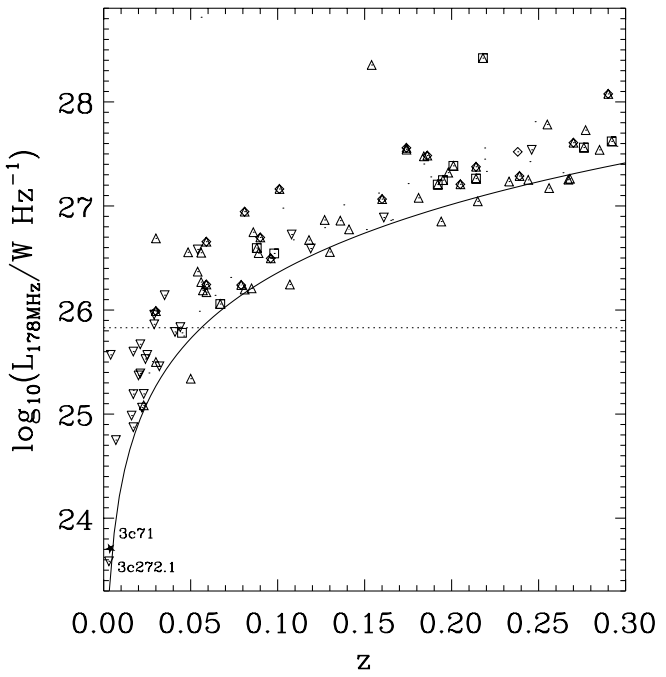

FIG. 1.—178 MHz radio luminosity of the sample. The dotted line indicates the conventional radio-loud/radio-quiet cutoff for quasars ($L_{5\,\mathrm{GHz}} = 10^{-24}$ W Hz^{-1} sr^{-1}), converted to 178 MHz assuming a power-law index of 1 for the radio luminosity ($L_\nu \sim \nu^{-1}$). The solid line indicates the (9 Jy at 178 MHz) flux limit of the 3CR survey. Note that two of the most well-known low-redshift targets, 3C 71 (M77, NGC 1068), and 3C 272.1 (M84, NGC 4374) actually fall below the radio-loud quasar cutoff. Upward-pointing triangles represent FR II's; downward-pointing triangles represent FR I's; diamonds represent high excitation galaxies (HEGs); squares represent low-excitation galaxies (LEGs). The single solid star represents 3C 71.

We retrieved the data, preprocessed through the standard calibration pipeline, from the MAST. We performed the data reduction described below using the Space Telescope Data Analysis System (STSDAS) software running under PyRAF. Two anomalies not removed by the calibration pipeline are corrected during our data reduction: the pedestal effect and the coronographic hole. NIC2 has a quadrant offset bias known as the pedestal effect (Noll et al. 2004). We use the task `pedsub` to remove this source of error. The task `pedsub` eliminates the pedestal effect but leaves the sky level untouched. We found that using `pedsky` on nearby sources (as in Paper I) led to some errors in the photometry due to inaccurate characterization and subtraction of the background flux. The NICMOS coronographic spot appears as a small, well-defined region of erroneous flux on each individual dithered image, and it is simply masked out before combining the images.

Each object was observed using a square dither pattern with four exposures of 288 s each (1152 s total integration time on each source). We use `Multidrizzle`, a one-step task to perform image combination, dithering and cosmic ray rejection (Koekemoer et al. 2002). We set `Multidrizzle` to leave the NIC2 native pixel size of 0.075″ and to not perform sky subtraction. Note that `Multidrizzle` produces a final output image in units of electrons per second. We convert to DN before proceeding, by dividing the images by the analog-to-digital conversion (ADC) gain and multiplying by the integration time, obtained from the relevant FITS image headers (ADCGAIN and EXPTIME, respectively). Also note that the default behavior of `multidrizzle` is to output weight maps that are exposure time maps. We adjusted this by setting `final_wht_type = ''ERR''` to produce inverse-variance maps.

For each source we have *k*-corrected the apparent magnitudes to rest-frame *H* band assuming a spectral index of $\alpha = 1.5$ for the host galaxy and $\alpha = 0.2$ for the nucleus where necessary ($f_\nu \propto \nu^{-\alpha}$). Galactic extinction corrections have been applied

TABLE 3
Radio Properties of the NICMOS Snapshot Survey Sample

Source	z	V	S(178 MHz)[a]/Jy	log P_{178}	α[a]	LAS[b,c]	P.A.[b,c]	FR[a]	Class[d]	$L_{O\,II}$[d]	$L_{O\,III}$[d]
3C 15	0.073	15.3	15.8	26.3	0.64	...	...	...	...	...	...
3C 17	0.219	18.0	20.0	27.4	0.52	...	...	...	...	...	...
3C 20	0.174	19.0	42.9	27.6	0.67	51	101	2	HEG	33.99	34.47
3C 28	0.195	17.6	16.3	27.2	1.06	30	166	2	LEG	35.07	...
3C 29	0.044	14.1	15.1	25.8	0.50	139	160	1	...	...	...
3C 31	0.016	12.1	16.8	25.0	0.57	1833	159	1	FRI	...	...
3C 33	0.059	15.2	54.4	26.7	0.76	...	...	2	HEG	34.72	35.37
3C 33.1	0.181	19.5	13.0	27.1	0.62	216	45	2	WQ	...	35.05
3C 35	0.067	15.6	10.5	26.1	0.77	704	12	2	LEG	...	...
3C 52	0.285	18.5	13.5	27.5	0.62	51	20	2	...	...	...
3C 61.1	0.186	19.0	31.2	27.5	0.77	186	2	2	HEG	34.70	35.48
3C 66B	0.021	12.9	24.6	25.4	0.62	330	54	1	FRI	33.16	33.01
3C 71	0.004	8.9	16.1	23.7	0.55	...	...	...	...	...	...
3C 75N	0.024	13.6	25.8	25.5	0.71	692	111	1	...	...	...
3C 76.1	0.032	14.9	12.2	25.5	0.77	200	...	1	FRI	...	...

Notes.—Main radio and optical properties for each source: redshift; V-band magnitude; radio flux density in janskys at 178 MHz; radio power at 178 MHz in W Hz^{-1}; radio spectral index; radio source largest angular size; radio structure position angle; Faranoff-Riley class; Ionization Class; [O II] λ3727 emission line luminosity in W; [O III] λ5007 emission line luminosity in W. Table 3 is available in its entirety in the electronic edition of the *Astrophysical Journal Supplement*. A portion is shown here for guidance regarding its form and content.

[a] Spinrad et al. (1985)—updated values were taken from the NASA Extragalactic Database (NED).
[b] de Koff et al. (1996) and references therein.
[c] Martel et al. (1999) and references therein.
[d] Jackson & Rawlings (1997).

following Schlegel et al. (1998). We assume throughout a flat, Λ-dominated cosmology in which $\Omega_\Lambda = 0.7$ and $h_0 = 0.7$.

3. MODELING PROCEDURE

We have used Ellipse (Jedrzejewski 1987) and Galfit (Peng et al. 2002) to model each source in the sample. The steps required to implement these models properly are outlined below (§ 3.1). To the elliptical isophotal values returned by Ellipse, we fit 1D Sérsic-law quasi-radial profiles (§ 3.2). Properties of these profiles are compared to those obtained by direct 2D fitting to the image data using Galfit (§ 3.3). We make use of the summary of photometric galaxy relationships by Caon et al. (1993) to convert between surface brightness, scale length, and total flux for different values of Sérsic index, n.

3.1. *Premodeling*

3.1.1. *Masks*

We began by creating a mask and error frame for each target, using the output weight frame and hot pixel flags from `Multidrizzle`. The input bad pixel masks are combined by `Multidrizzle` to produce a final mask of all hot or bad pixels. To this we added an additional source mask to remove any external sources, companions, diffraction spikes, and the warm (ampglow-affected) corners of the image from the fit. These masks were applied to all the subsequent fits described below.

3.1.2. *Errors*

The combined weight ($1/\sigma^2$) frames that are output by `Multidrizzle` incorporate the Poisson noise and read noise on each pixel. We converted them to standard error (σ) frames. For the nuclear-dominated sources (with nuclei providing $\gtrsim$50% of the total flux), the errors are dominated not by Poisson or read noise, but by the "sampling error" associated with the lack of knowledge of the point spread function (PSF). In these cases we follow the technique described in Floyd et al. (2004) to provide accurate representation and weighting across the entire dynamic range, from the nucleus to the wings of the PSF. In practice, this means estimating the "sampling error" in concentric circular annuli, centered on the nuclei, from the deviation of the source from the PSF within each annulus. Where this drops to the Poissonian level (typically within a radius of $\sim$0.5″), we revert to the properly calculated individual pixel errors described above.

3.1.3. *Point Spread Functions*

Point spread functions (PSFs) were calculated for each target using `Tinytim` (Krist 1999), setting the position of the PSF to the average of the four central positions of the target. We generated a PSF at twice the resolution of the NIC2 chip, to provide oversampling and accurate shifting and convolution. Defocus was estimated for the time of each observation using the tables and figures provided on the NICMOS Web site,[10] and this information was included in each `Tinytim` model. The `Tinytim` models were, last of all, rotated through the same angle as the target images, to give north up in each case.

3.1.4. *Sky Background Level*

For all targets, an initial measurement of the approximate background level in the image was made using `imstatistics` to determine the photometric statistics on several empty regions of the chip. We attempted to measure the background in all four quadrants of the chip, as a check of the success of the quadrant bias removal. In practice, on all images where this was possible, the quadrants were found to have identical backgrounds, within the Poissonian errors. On objects that are too close for us to observe any background on the small $19'' \times 19''$ NIC2 chip (in practice, almost all objects at $z < 0.1$ and some large objects at higher redshifts) we employed the technique developed by Sparks & Jorgensen (1993): All of these targets have been observed previously using WFPC2 in either R or V band (or both). We obtained the reduced full WFPC2 mosaics from the 3CR database[11] and

[10] See http://www.stsci.edu/hst/observatory/focus/documents.html.
[11] See http://acs.pha.jhu.edu/~martel/.

TABLE 4
ELLIPSE AND 1D SÉRSIC MODEL FITS

Source	$(1 - b/a)_{\rm med}$	$\theta_{\rm med}$	$a_3/a_{\rm min}$	$a_3/a_{\rm max}$	$a_4/a_{\rm min}$	$a_4/a_{\rm max}$	r_e/kpc	$\langle\mu\rangle_e$	n
3C 15	0.06	21.32	−0.08	0.02	−0.04	0.02	4.96 ± 0.45	19.76 ± 0.13	4.17 ± 0.08
3C 17	0.17	21.32	−0.17	0.06	−0.08	0.14	5.84 ± 1.53	20.69 ± 0.52	10.00 ± 0.00
3C 20	0.10	−63.77	−0.06	0.10	−0.03	0.20	2.72 ± 1.45	19.17 ± 1.05	3.23 ± 0.54
3C 28	0.18	−26.43	−0.03	0.11	−0.04	0.03	6.74 ± 0.63	20.26 ± 0.11	2.01 ± 0.08
3C 29	0.03	−76.28	−0.05	0.02	−0.05	0.03	4.44 ± 0.15	19.05 ± 0.02	1.50 ± 0.02
3C 31	0.12	−32.23	−0.02	0.08	−0.03	0.01	1.46 ± 0.05	17.20 ± 0.02	1.43 ± 0.02
3C 33	0.07	−43.84	−0.09	0.01	−0.04	0.06	2.75 ± 0.21	18.97 ± 0.11	3.19 ± 0.07
3C 33.1	0.06	13.96	−0.02	0.03	−0.05	0.02	2.19 ± 0.65	18.66 ± 0.65	4.49 ± 0.33
3C 35	0.23	−65.28	−0.18	0.02	−0.07	0.03	4.59 ± 0.67	19.89 ± 0.20	3.60 ± 0.14
3C 52	0.31	10.96	−0.03	0.06	−0.02	0.08	3.55 ± 0.36	18.74 ± 0.18	1.73 ± 0.09
3C 61.1	0.09	0.95	−0.17	0.22	−0.07	0.08	1.87 ± 0.16	19.65 ± 0.20	2.07 ± 0.11
3C 66B	0.06	−50.32	−0.08	0.04	−0.03	0.06	2.42 ± 0.15	18.42 ± 0.04	1.97 ± 0.05
3C 71	0.18	36.54	−0.04	0.03	−0.06	0.02	2.21 ± 0.51	19.51 ± 0.35	10.00 ± 0.00
3C 75N	0.19	−80.47	−0.01	0.05	−0.02	0.04	1.64 ± 0.22	17.75 ± 0.16	3.09 ± 0.12
3C 76.1	0.14	−47.79	−0.02	0.04	−0.05	0.02	1.12 ± 0.07	17.95 ± 0.09	2.26 ± 0.06

NOTES.—Columns list properties of the elliptical isophotal fit to each source, including 1D radial-profile Sérsic fit: median ellipticity; median position angle (east of north); minimum value of a_3/a; maximum value of a_3/a; minimum value of a_4/a; maximum value of a_4/a. scale length (half-light radius) of best-fit model to elliptical isophotes; mean surface brightness of model within scale length, $\langle\mu\rangle_e$; Sérsic index of model. Table 4 is available in its entirety in the electronic edition of the *Astrophysical Journal Supplement*. A portion is shown here for guidance regarding its form and content.

measured the background flux on these larger images. Profiles of the flux in each of the two bands were produced and plotted against each other. In all cases there is a region of linearity in the two flux levels, and a linear fit was made in this region, extrapolating down to obtain the IR flux at the level of the optical (WFPC2) background. As a check of the robustness of this fitting technique, we also deployed it on images of five higher redshift sources, where a clear measurement of the infrared background was also possible from the NIC2 image. In these cases we produced a small cutout of the infrared image, such that no background light was visible, mimicking the situation for the lower redshift targets. In these tests, all five fits yielded infrared backgrounds that again were within the Poissonian error of the true, measured background fluxes on the original infrared images.

3.2. *Ellipse Fitting*

We used the `Ellipse` modeling procedure in `Iraf.stsdas` to fit elliptical isophotes to the sky-subtracted NICMOS images. We initialized each fit by feeding it the position of the centroid of the source, as measured using `imcntr`, and estimated values of the position angle (P.A.) and ellipticity ($1 - b/a$). We began the fit at 10 pixels (semimajor axis length) working outward in geometric steps, increasing in size by a factor of 1.1. Once the fit has terminated due to insufficient pixels (less than half on a given annulus, `fflag` = 0.5), or convergence (largest harmonic amplitude <5% of the residual rms around the harmonic fit) it returns to fit the inner region with identical geometric steps, all the way to the center of the target. The central position, ellipticity, and P.A. of each ellipse were left free to explore the stability of the isophotal centering and investigate structures in the galaxy deviating from the purely elliptical. Deviation from a perfect ellipse at each radius is broken down with a Fourier series, characterized by the third- and fourth-order sine and cosine coefficients. We convert from the `ellipse` parameters A3, A4, B3, and B4 to a_4/a, b_4/b following the conversion described in Milvang-Jensen & Jørgensen (1999; see that paper for a useful discussion of all the ellipse fit parameters). Additional masking was performed, in software, on pixels deviating by more than 3 $\sigma_{\rm annulus}$ from the mean value on a given fitted elliptical annulus.

Modeling with `ellipse` allows us to track radial changes in the ellipticity and position angle of the isophotes of galaxies, providing a powerful analysis of the structure of the galaxy, and the presence of any disturbances from a relaxed elliptical morphology. One-dimensional Sérsic (1968) profile fits were made to the best-fitting ellipse-isophotal intensities, after convolution of the model with a point-spread function (PSF), using a Levenberg-Marquardt nonlinear least-squares minimization technique (Press et al. 1992). This technique has been widely used in the past for studying the properties of elliptical galaxies (e.g., Bender et al. 1992; Graham et al. 1996) and mergers (e.g., Rothberg & Joseph 2004), but note that it does not provide a true "radial profile" since adjacent elliptical isophotes may have different position angles and ellipticities, thus overlapping, and contributing flux to one another. For purposes of comparison with the 2D fits (see below) and with the literature, the median values of ellipticity, position angle, and diskiness were computed for the isophotal fits between a radius of 0.5″ (inside of which the nucleus may dominate) and where the signal drops to 3 $\sigma_{\rm sky}$, or the edge of the chip if that is reached first. The results of the elliptical isophote fitting are presented in Table 4.

3.3. *Galfit*

Galfit (Peng et al. 2002) is a versatile fitting code that allows the user to fit multiple components to a galaxy in an iterative fashion, using a downhill gradient Levenberg-Marquardt technique. The model galaxy is convolved with a PSF at each iteration and compared to the data through the χ^2 statistic. We fitted each object using a single Sérsic component convolved with a PSF, plus an additional unresolved nuclear component represented by the same PSF. Error frames and masks were produced as described in § 3.1.2 above. The majority of objects are too distant to allow detection of a "Nuker" (e.g., Faber et al. 1997) or Graham et al. (2003) type core, so we adopt just a single Sérsic component for study throughout the sample for consistency, simplicity, and comparison with the bulk of the literature.

The complete (Sérsic + PSF + sky) model has 11 free parameters: center of host (x, y); luminosity of the host galaxy (L_H); scale length of the host galaxy (R_e); position angle of the host galaxy (θ); ellipticity of the host galaxy (b/a); Sérsic parameter

TABLE 5
2D Sérsic Model Fits

Source	M_H(Nuc)	M_H(Host)	R_e/kpc	μ_H	n	$1-(b/a)$	θ	d
3C 15	...	−24.33 ± 0.01	8.41 ± 0.05	18.86 ± 0.01	6.10 ± 0.02	0.07 ± 0.00	19.33 ± 0.38	0.11 ± 0.01
3C 17	−21.51	−24.19 ± 0.01	4.25 ± 0.05	17.52 ± 0.00	7.49 ± 0.11	0.23 ± 0.00	20.94 ± 0.31	−0.21 ± 0.02
3C 20	...	−23.61 ± 0.00	2.19 ± 0.01	16.66 ± 0.00	2.70 ± 0.01	0.10 ± 0.00	−65.53 ± 0.62	−0.15 ± 0.01
3C 28	−18.71	−24.70 ± 0.01	11.12 ± 0.07	19.10 ± 0.01	2.32 ± 0.02	0.24 ± 0.00	−33.50 ± 0.23	−0.26 ± 0.01
3C 29	−16.19	−23.82 ± 0.01	4.24 ± 0.01	17.89 ± 0.01	1.45 ± 0.00	0.04 ± 0.00	−81.55 ± 0.00	0.08 ± 0.00
3C 31	...	−23.29 ± 0.00	1.72 ± 0.00	16.46 ± 0.00	1.67 ± 0.00	0.12 ± 0.00	−32.98 ± 0.08	−0.01 ± 0.00
3C 33	...	−23.43 ± 0.00	2.98 ± 0.01	17.51 ± 0.00	3.60 ± 0.01	0.08 ± 0.00	−35.60 ± 0.26	−0.13 ± 0.01
3C 33.1	−20.86	−23.84 ± 0.02	2.68 ± 0.02	16.86 ± 0.02	6.41 ± 0.00	0.01 ± 0.01	54.91 ± 2.56	0.00 ± 0.00
3C 35	...	−24.07 ± 0.00	8.38 ± 0.04	19.11 ± 0.00	4.79 ± 0.01	0.28 ± 0.00	−66.34 ± 0.07	−0.02 ± 0.00
3C 52	...	−25.06 ± 0.00	5.22 ± 0.02	17.10 ± 0.00	2.49 ± 0.01	0.35 ± 0.00	10.16 ± 0.18	−0.17 ± 0.02
3C 61.1	−16.96	−22.18 ± 0.11	1.73 ± 1.56	17.59 ± 0.00	2.83 ± 0.00	0.13 ± 0.01	−2.02 ± 1.22	0.41 ± 0.00
3C 66B	...	−23.35 ± 0.01	2.93 ± 0.01	17.56 ± 0.01	2.39 ± 0.01	0.07 ± 0.00	−59.24 ± 0.34	0.00 ± 0.00
3C 71	...	0.86 ± 0.01	1.17 ± 0.01	39.77 ± 0.00	3.12 ± 0.02	0.38 ± 0.00	44.99 ± 0.09	0.00 ± 0.00
3C 75N	...	−23.35 ± 0.00	1.68 ± 0.00	16.34 ± 0.00	3.68 ± 0.01	0.14 ± 0.00	−78.88 ± 0.15	0.22 ± 0.01
3C 76.1	...	−22.28 ± 0.00	1.31 ± 0.00	16.88 ± 0.00	2.95 ± 0.00	0.16 ± 0.00	−48.12 ± 0.12	−0.08 ± 0.00

Notes.—Columns list properties of the best-fit 2D Sérsic model to each source: absolute magnitudes of the nucleus and host galaxy; scale length (half-light radius) in kpc R_e; surface brightness at the scale length μ; Sérsic index n; ellipticity $1-(b/a)$; position angle θ (relative to north); diskiness, d. Notes: The following objects did not admit a complete or normal fit, as discussed in the main text: (a) 3C 71 is too extended to be properly constrained on either the NIC2 or WFPC2 chips; (b) 3C 258—values are presented as if the target lay at $z = 0.165$—however, it is likely that the source is actually at higher redshift. Table 5 is available in its entirety in the electronic edition of the *Astrophysical Journal Supplement*. A portion is shown here for guidance regarding its form and content.

of the host galaxy (n); luminosity of the nucleus (L_N); position of nucleus (x, y); and background flux. We initially held fixed the values of the Sérsic index ($n = 4$; i.e., a de Vaucouleurs elliptical), the "diskiness" parameter, ($c = 0$), and the sky background flux (at a level determined as described in § 3.1.4). After a satisfactory fit was obtained, we freed these parameters one by one, in an iterative modeling procedure, in the order listed above. Last of all, the sky value was freed up to see if a better fit could be obtained and to test the degeneracy between sky background and host galaxy flux. The models presented here include this fitted sky value, which was always consistent with the measured sky value. The results of the Galfit Sérsic model fitting are presented in Table 5.

As discussed above (§ 3.1.2), we have adopted the error analysis technique of Floyd et al. (2004) for nuclear-dominated objects. Since this is not the standard error treatment used by Galfit, we performed extensive tests (discussed in the Appendix) of the effect of this assumption on the fits produced by Galfit using both real and synthetic sources. We found Galfit produced identical results using each technique for sources with weaker nuclei. We argue that the Floyd et al. (2004) technique is the formally correct analysis of the errors for sources with dominant nuclei since it properly accounts for all sources of error across the image.

3.4. *Errors on the Fitted Parameters*

Errors on the fitted parameters in each case are calculated from the diagonal elements of covariance matrix for that set of parameters, following the assumption that each parameter is independent. The errors quoted in Tables 5 and 4 are formal 1 σ statistical errors. Note that in many cases, the true errors are dominated by the systematics, since the galaxies are not ideal. To investigate this, we performed simple tests of different galaxy fitting algorithms as described in the Appendix. Including all systematics, we expect that all our morphological results are accurate to within 10% and host fluxes within 2%.

4. NOTES ON INDIVIDUAL OBJECTS

In this section we present notes and images for the newly observed objects in our SNAP program (i.e., those not included in Paper I) in Figure 2, and those taken from the archive in Figure 3.

4.1. *Newly Observed Sources*

4.1.1. *3C 15; $z = 0.073$*

This source exhibits a prominent optical-IR jet (Martel et al. 1998) in an apparently undisturbed round elliptical that almost fills the NICMOS2 field of view. No bright nuclear point source is detectable in the H band.

4.1.2. *3C 17; $z = 0.219$*

This very peculiar radio source (Morganti et al. 1999) and BLRG has a quite round elliptical galaxy and a prominent IR nucleus. There are several faint companions in the immediate surroundings of the host galaxy.

4.1.3. *3C 33; $z = 0.059$*

An FR II HEG source with a prominent dust disk aligned $\sim 45^\circ$ to the radio axis. The host galaxy is elliptical, appearing slightly disturbed due to the dust disk.

4.1.4. *3C 98; $z = 0.030$*

A NLRG FR I, hosted by an undisturbed elliptical with smaller companion elliptical. No internal structure is visible in the NICMOS2 image. The radio source is double lobed, running almost north–south (Miller 1985).

4.1.5. *3C 132; $z = 0.214$*

3C 132 appears near the western corner of the NIC2 image, and has a somewhat elongated, smooth elliptical host galaxy. Several companions are visible, including one bright foreground star at the image center. The radio axis of this FR II source is almost perpendicular to the major axis of the host galaxy.

4.1.6. *3C 153; $z = 0.277$*

3C 153 is a radio galaxy (angular size $6'' = 25$ kpc) oriented at P.A. of $\sim 50^\circ$ with an FR II radio morphology and a large arm-length ratio ~ 1.9 (Laing 1981). It has been classified as a CSS

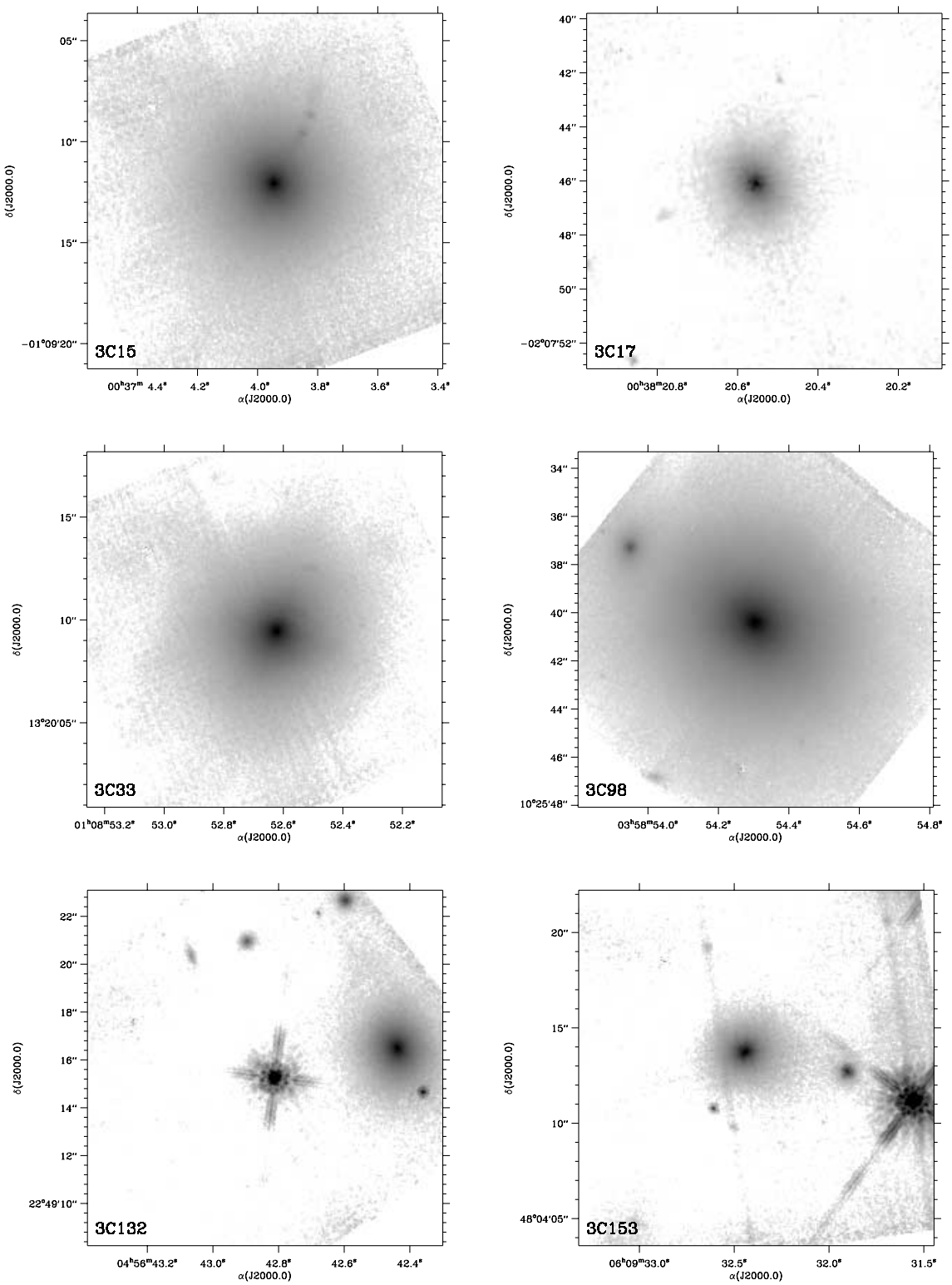

FIG. 2.—NICMOS2 f160w (*H* band) images of the newly observed objects aligned north up (see Table 1).

source (e.g., Akujor et al. 1991) but it would be at the upper end of the size distribution for such sources. The [O II] emission line nebula is slightly extended along the radio axis (McCarthy et al. 1995). de Koff et al. (1996) note that the galaxy has an elliptical nucleus and strong emission lines. The NICMOS image shows a fairly round host galaxy. There are a couple of unresolved sources nearby but they do not correlate with knots or hotspots in the radio source. Two other features are caused by the intersection of diffraction spikes.

4.1.7. *3C 166; z* = 0.245

An unusual radio source featuring two lobes with very different morphologies (Spangler & Bridle 1982). The radio axis runs north–south, with Spangler & Bridle's southern features C and D

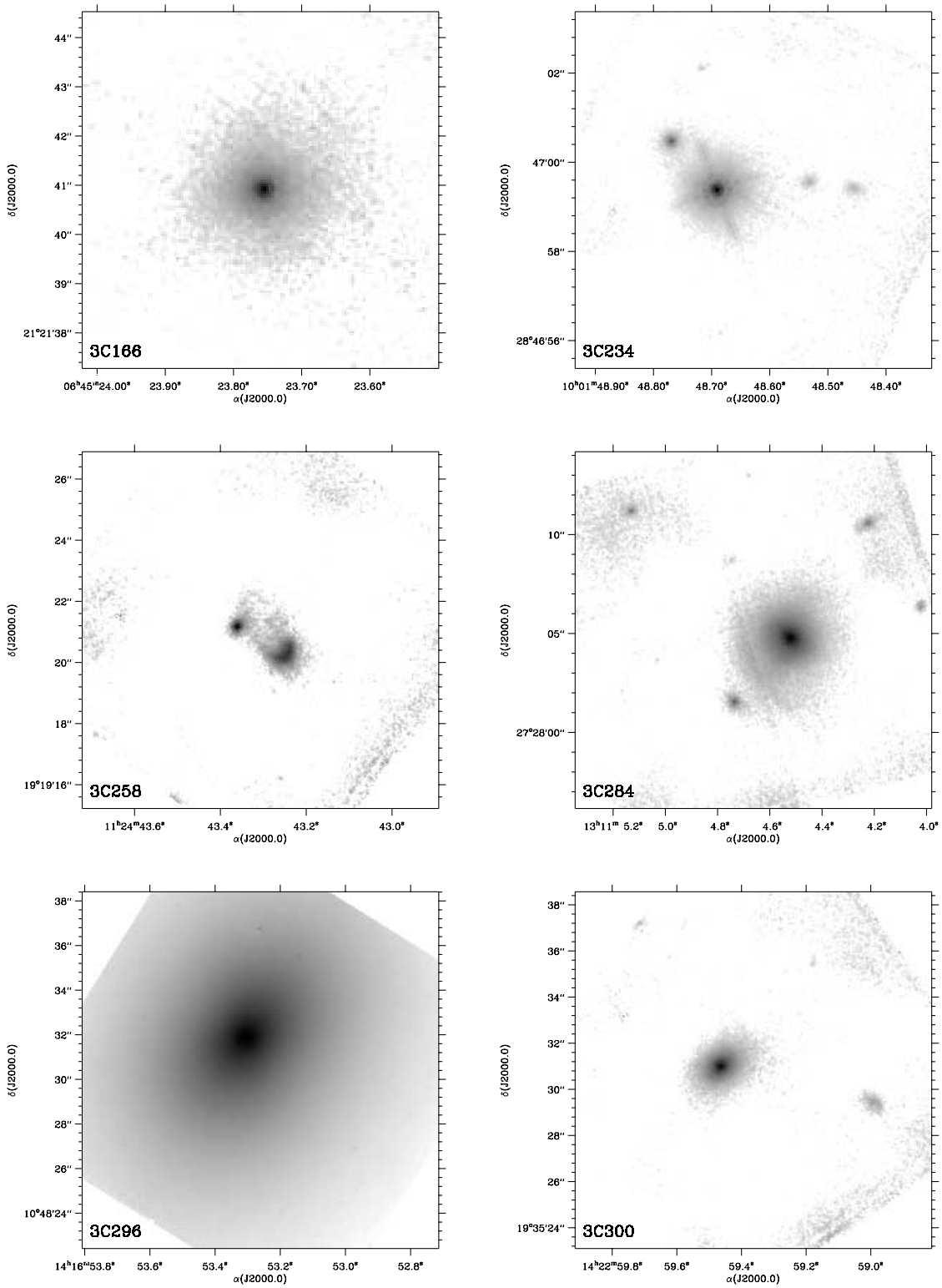

FIG. 2—*Continued*

detected on the IR image as infrared hotspots. The source has a clearly detected, unresolved infrared nucleus.

4.1.8. *3C 234; z* = 0.185

3C 234 exhibits a bright quasar-like nucleus in the NICMOS image, and is known to be a broad-line radio galaxy (McCarthy et al. 1995) with a classical double FR II radio source. In the optical (de Koff et al. 1996; McLure et al. 1999) there are features emanating from the nucleus in the east and west direction. The western feature, described as a tidal arm by McLure et al. is detectable on the new NICMOS image. There are two additional sources to the west in the same direction, the furthest of which is also detectable in F555W and F702W. Both are detectable in F675W. This galaxy is known to have strong extended emission

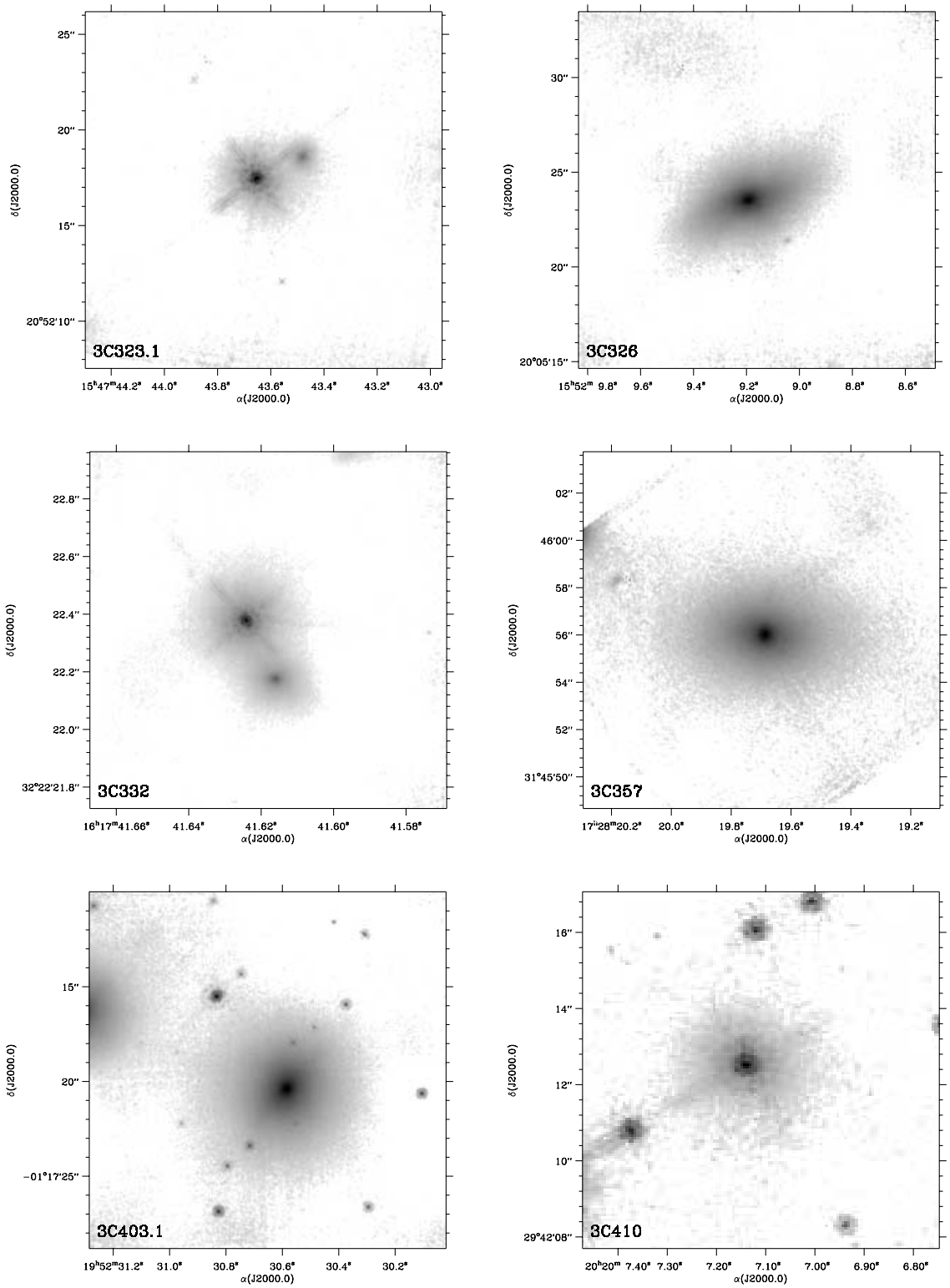

FIG. 2—*Continued*

lines that likely explain these features. Paβ (1.28 μm) is in the passband of F160W at the redshift of 3C 234.

4.1.9. *3C 258; $z = 0.165$*

This galaxy is a well-known compact steep-spectrum (CSS) radio source, with a compact, double radio structure seen on scales of a few tenths of an arcsecond along P.A. $\approx 33^\circ$ (Spencer et al. 1989; Akujor et al. 1991; Ludke et al. 1998), although its arcminute scale structure is aligned along a nearly north–south direction Strom et al. (1990). Its redshift has been quoted as $z = 0.165$ (Smith et al. 1976), but this value is in dispute, as Dey (1994) note that spectra taken at Lick show a likely background quasar, based on the observation of a single emission line at 7111 Å, which would give $z = 1.54$ if due to Mg II λ2798.

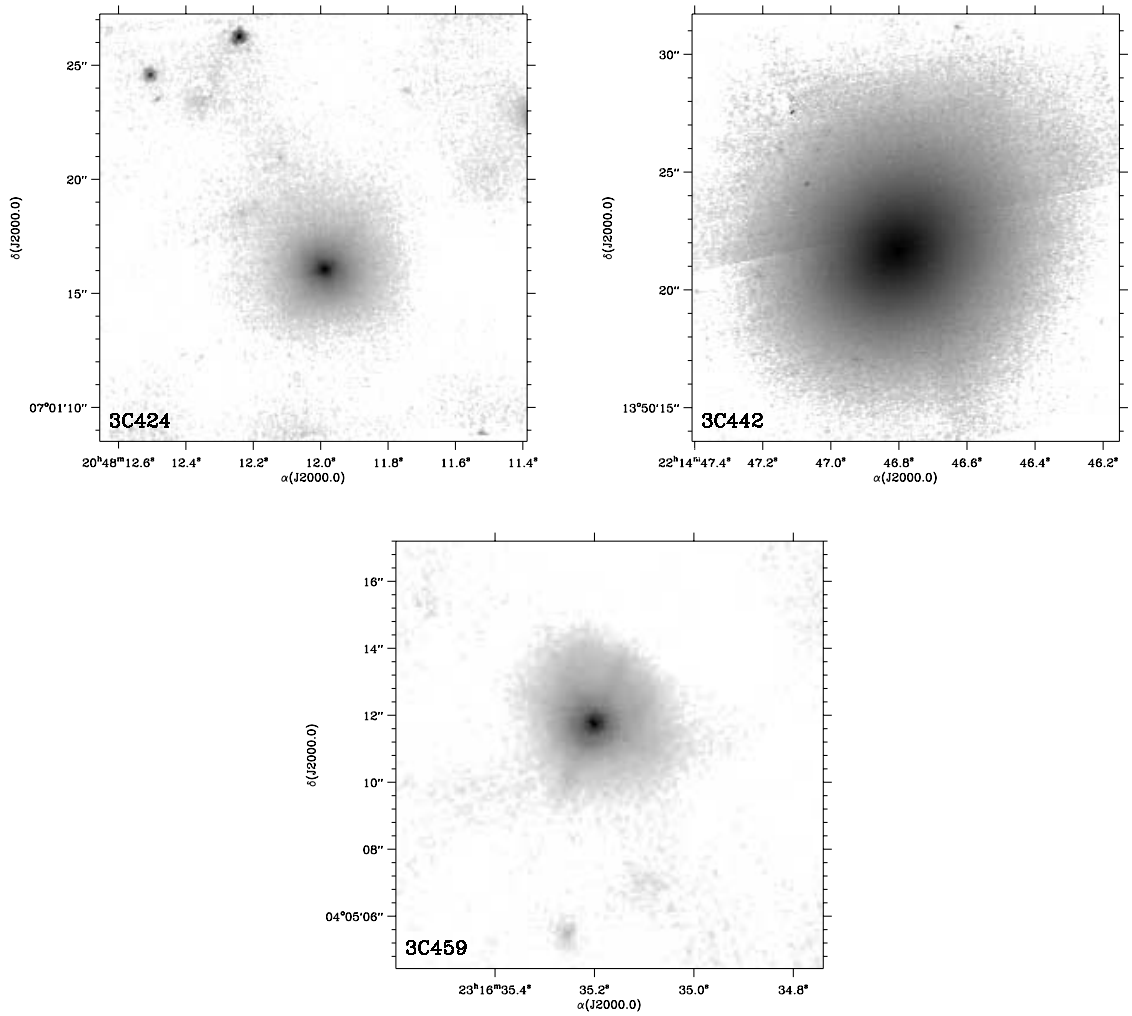

FIG. 2—*Continued*

However, due to poor seeing at the time the spectra were taken, no firm claims can be made as to the origin of this line. Our NICMOS data are consistent with a significantly higher redshift, as they show a very compact host galaxy that is much fainter than one would expect for an object at $z = 0.165$. The nuclear point source in our image is also quite bright, with an arc-like object 3″ east-southest of the AGN that may be an irregular foreground ($z = 0.165$) galaxy causing the confusion.

4.1.10. *3C 284;* $z = 0.239$

An FR II HEG radio source, hosted by a disturbed elliptical with a southeast tidal tail toward its most prominent companion 4″southeast. Several fainter companions are also visible on the NICMOS chip. In the optical the source has a disky appearance and double nucleus, owing to this same tidal tail and associated dust lanes.

4.1.11. *3C 296;* $z = 0.025$

3C 296 is hosted by an extremely boxy elliptical galaxy. It has a double-lobed jet with clear radio emission along the jet axis (FR I). The WFPC2 image (Martel et al. 1999) shows a truncated edge-on disk embedded in the galaxy, similar to that seen in NGC 4261. The disk is aligned with the major axis of the elliptical galaxy, with the jet perpendicular to the disk. The nucleus is seen in both WFPC2 image (although faint) and in the NICMOS image (brighter). X-ray and radio observations of this galaxy are discussed in Hardcastle et al. (2005).

4.1.12. *3C 300;* $z = 0.270$

A double-sided FR II HEG, hosted by a compact, elongated ~3 kpc elliptical host galaxy with a faint companion 8″ east, and a very faint tidal distortion. The radio axis runs roughly southeast-northwest, and there is a faint thread of emission along this axis on the northwest side, which is a candidate jet. However, it is almost lost in the noise of the NICMOS chip edge.

4.1.13. *3C 323.1;* $z = 0.264$

This QSO has a bright nucleus that produces diffraction spikes in the near-infrared image. It has a close companion to the northwest that does not show clear signs of interaction, but is consistent with being the remnant nucleus of a galaxy in the final stages of merging (Miller & Sheinis 2003; Canalizo & Stockton 1997). The Keck spectroscopy presented by Miller et al. demonstrate that the host is not a normal elliptical galaxy, and from our *H*-band image there is some evidence of disturbance, which may explain the small scale length fit to the data. It is also possible that the radio emission from this source is Doppler boosted, making it an artificially radio-loud object.

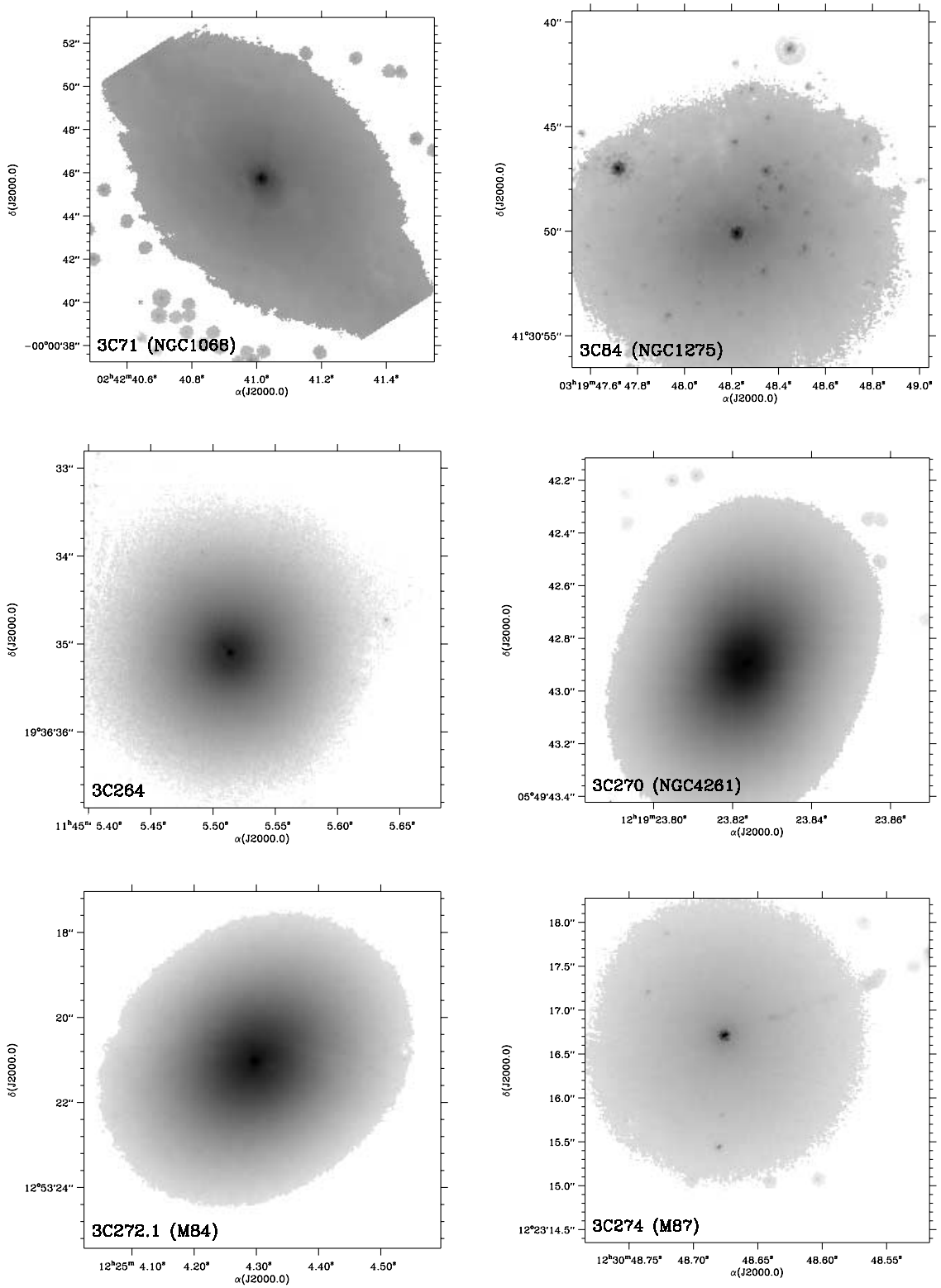

FIG. 3.—NICMOS2 f160w (*H* band) images of the archival objects (see Table 2).

4.1.14. *3C 326; z* = 0.090

A double source, the new NICMOS image shows only the southern, which is the stronger of the two in the radio (Rawlings et al. 1991). A larger companion elliptical sits 25″(43 kpc) to the north. A dust disk bisects the nucleus of the small elliptical host galaxy, giving the appearance of a disk. Three very faint small companion sources are visible within or close to the main galaxy halo. Unusually, the radio axis is aligned close to the axis of the disk.

4.1.15. *3C 332; z* = 0.270

A powerful FR II radio galaxy with a prominent quasar-like infrared nucleus marking the center of an elliptical host galaxy. There is a smaller companion 3″to the southwest.

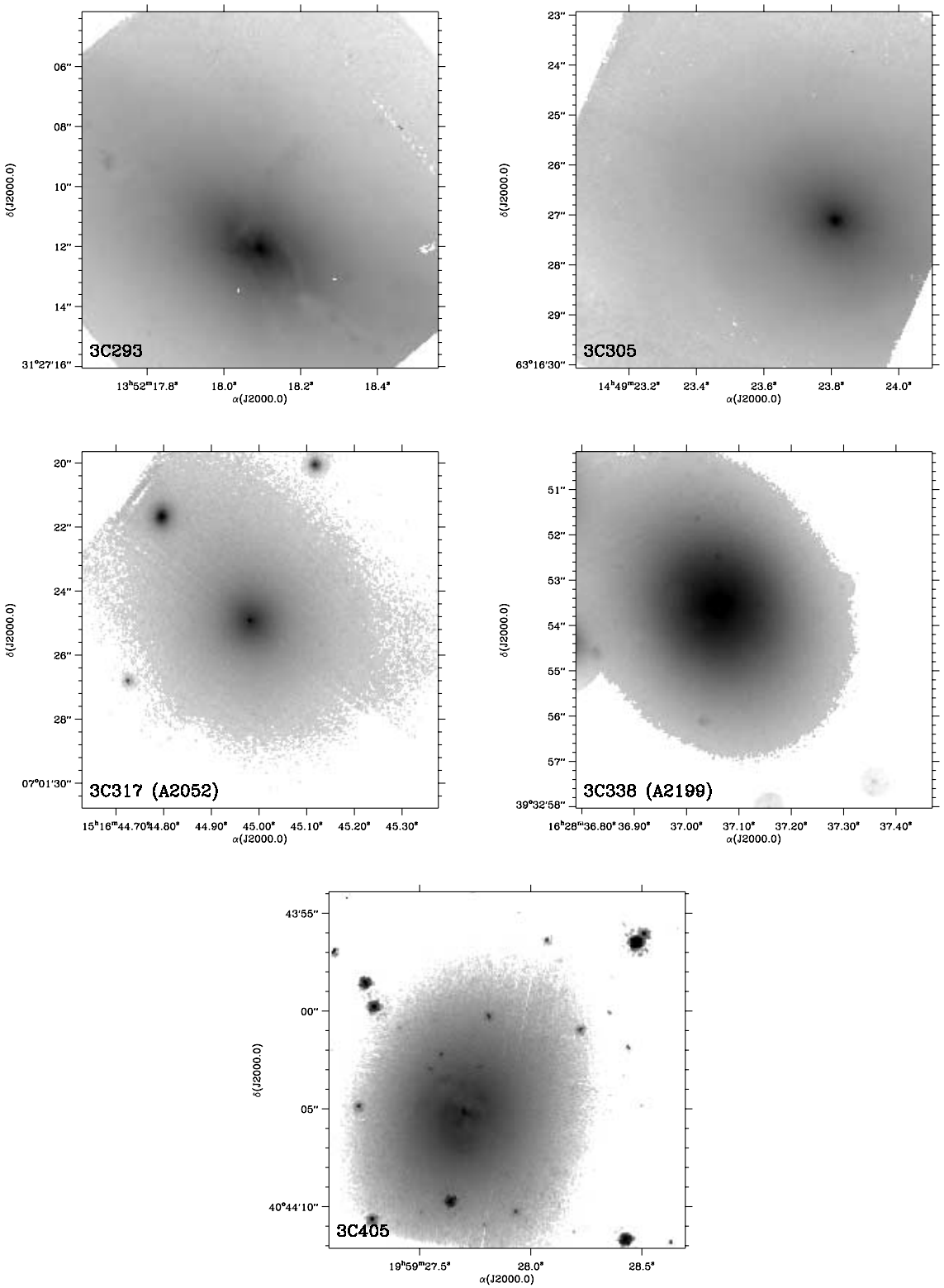

FIG. 3—*Continued*

4.1.16. *3C 357; z* = 0.166

3C 357 is an FR II radio galaxy with angular size 90″(250 kpc) at a P.A. 110° (Fanti et al. 1987; Harvanek & Hardcastle 1998). In both lobes the hotspots are off to one side, suggesting there has been a change in the jet direction. There is emission-line gas extending a few arcsec from the nucleus along the radio axis (McCarthy et al. 1995). de Koff et al. (1996) and Capetti et al. (2000a) note that there are filamentary dust lanes southwest of the nucleus. The galaxy isophotes are very elliptical with no remarkable features. There is a single faint candidate companion source 8″ east, with a larger companion just on the eastern edge

of the chip. No unresolved nucleus is detected, but the core of the galaxy appears unusually bright, and the host has a high Sérsic index ($n = 5.34$).

4.1.17. *3C 403.1; $z = 0.055$*

This double radio source lies at low Galactic latitude ($b \approx -14^\circ$), resulting in numerous stars on the image. In spite of this one can see that the undisturbed-looking elliptical host galaxy is located in a fairly dense environment, with one large companion seen on the NICMOS chip and three others similar in brightness visible on the WFPC2 (Martel et al. 1999) image.

4.1.18. *3C 410; $z = 0.248$*

Our observations of 3C 410 suffered a pointing error, resulting in only two usable images of the source—hence, the rather noisy image. A strong central nuclear point source is visible centered on a round elliptical host galaxy. Numerous unresolved sources are visible in the field.

4.1.19. *3C 424; $z = 0.127$*

Faint tidal distortions are visible to the north on our NICMOS image, and this source lies in a dense environment, with numerous large companions visible on the WFPC2 (de Koff et al. 1996) image. The radio source apparently lies on the edge of the cluster. Two bright unresolved sources are visible to the north, with a resolved object northwest, on the edge of the NICMOS chip, barely detected at *R*.

4.1.20. *3C 442; $z = 0.026$*

Only two exposures can be used of the four, due to telescope pointing errors. The host galaxy is a smooth elliptical, with two companions visible on the WFPC2 image (Martel et al. 1999). The point source on the edge of the NICMOS chip to the west-southwest is in line with the radio axis and is a candidate hotspot—also clearly visible on the WFPC2 images.

4.1.21. *3C 459; $z = 0.219$*

A strong IR nucleus and heavily distorted off-center host galaxy distinguish this FR II radio galaxy. The host is dominated by young stellar population (Tadhunter et al. 2002) and must have undergone a recent merger. The radio source is small (10″) and also very asymmetric (Morganti et al. 1999).

4.2. *Archival Data*

4.2.1. *3C 71 (NGC 1068, M77); $z = 0.003793$*

A well-known spiral galaxy, and the archetypal Seyfert 2, NGC 1068 is not truly "radio-loud" in terms of its radio luminosity. It has an obscured Sy 1 spectrum (Antonucci & Miller 1985) and a compact (few arcsec) radio jet aligned north-northeast–south-southwest. The NICMOS data were obtained as part of the NICMOS GTO time by Thompson & Corbin (1999). The galaxy dwarfs the small NIC2 chip and even the WFPC2 mosaic (PROPOSIDs 5479, 5754). We were unable to produce an accurate photometric fit to this object, since we could not estimate the background flux. The spiral structure and active nucleus are readily apparent on the NICMOS image, as are numerous globular clusters. There is a vast literature on this source.

4.2.2. *3C 84 (NGC 1275, Per A); $z = 0.017559$*

The central galaxy of the Perseus cluster contains an FR I radio source and Seyfert 2 nucleus at the center of a cooling flow. It shows a large number of companion sources in the infrared and a complicated dust morphology in the optical-IR. The NICMOS data were first published by Martini et al. (2003). Only the central region is visible in the NIC2 image. We used the F702W image from Martel et al. (1999) to estimate the background. However, due to the immense size of this cD galaxy, even the full WFPC2 mosaic (PROPOSID 6228) does not detect the edge of the galaxy, and the results are photometrically uncertain.

4.2.3. *3C 264; $z = 0.021718$*

3C 264 is a tailed radio source in the cluster Abell 1367.[12] On the arcsec scale there is a bright one-sided jet that is detected in the radio (Baum et al. 1997; Lara et al. 1999), optical (Crane et al. 1993), and X-ray (Tilak 2006; Padgett et al. 2005). Baum et al. (1997) note the existence of an inner dusty disk that causes an apparent ring in the galaxy surface brightness where the disk ends. The NICMOS image shows a bright nucleus, the jet and the ring noted by Baum et al. The data were previously published by Capetti et al. (2000b).

4.2.4. *3C 270 (NGC 4261); $z = 0.007465$*

A well-studied nearby FR I with a boxy elliptical host galaxy and a circumnuclear dust disk. Ferrarese et al. (1996) used imaging and spectroscopy of this source to determine its black-hole mass. A faint unresolved nuclear point source is visible in the IR. Data were first published by Quillen et al. (2000).

4.2.5. *3C 272.1 (NGC 4374, M84); $z = 0.003536$*

A large well-studied elliptical in the Virgo cluster with a prominent dust lane visible in the optical, and faintly detectable in the NICMOS image Bower et al. (2000). The radio source is a double-sided FR I jet and core. However, its radio power is somewhat lower than the fiducial cutoff for radio-loud quasars. It is described as a "weak radio galaxy" by Laing & Bridle (1987).

4.2.6. *3C 274 (NGC 4486, M87, Virgo A); $z = 0.004360$*

An FR I with celebrated optical jet. The NICMOS data were originally presented by (Corbin et al. 2002), where the source is studied in detail.

4.2.7. *3C 293 (UGC 08782); $z = 0.045034$*

A merger-remnant with significant distortion at optical and IR wavelengths. The prominent optical dust lanes partially cover an optical jet that is clearly seen in the infrared. This object was studied in detail by Floyd et al. (2006a).

4.2.8. *3C 305 (IC 1065; UGC 09553); $z = 0.041639$*

A nearby FR I and merger remnant, with prominent dust lane across the nucleus in the optical. Studied in detail by Jackson et al. (2003). The host galaxy is a large, elongated elliptical, with clear signs of disturbance in the optical and the IR. See Jackson et al. (2003) for original publication of the data and a detailed study of the object.

4.2.9. *3C 317 (Abell 2052; UGC 09799); $z = 0.034457$*

3C 317 is a slightly elongated elliptical with an unresolved nucleus. Two small elliptical galaxies are present in the field of view, one is located 7″ to the northeast, and the second one 9″ to the northwest. The image of this galaxy taken by Martel et al. (2002) shows a peculiar UV filament ~4 kpc south of the nucleus. This filament is described as a region of active star formation

[12] See http://www.jb.man.ac.uk/atlas/dragns.html.

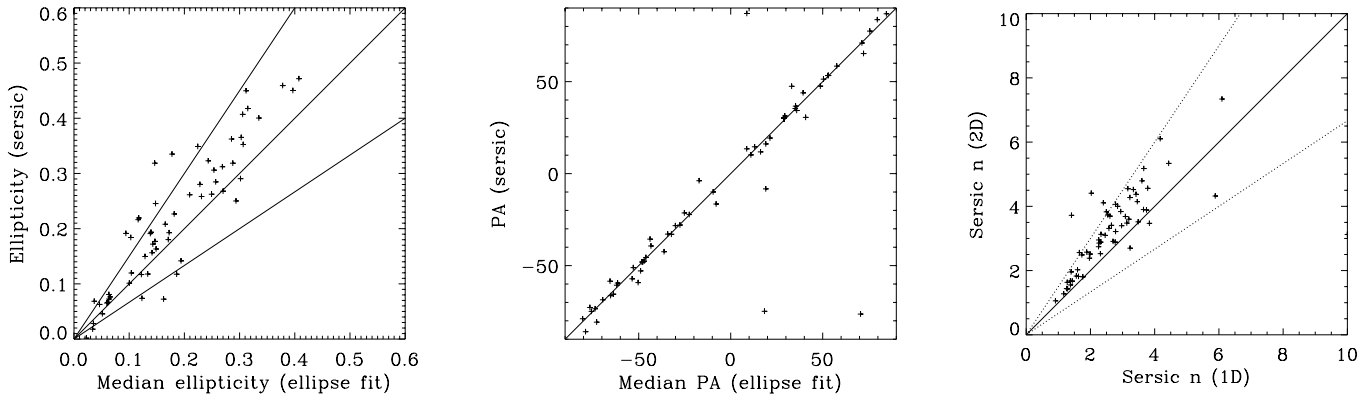

FIG. 4.—Results of the Ellipse (1D) and Galfit (2D) fits compared for targets without strong nuclear point sources (i.e., in which the nucleus contributes <10% of the total luminosity). *Left-to-right*: Ellipticity, position angle (P.A.), and Sérsic index. We plot the median ellipticity and P.A. of the ellipse fits, which are found to be consistent with the 2D parameters. The Sérsic profile indices, n, fitted to the elliptical isophotal intensities differ from those fitted directly to the data through the 2D parametric model by up to a factor of 1.5 (indicated by the dotted lines). The three outliers are 3C 88, 3C 296, and 3C 338.

likely triggered by a recent merger by Martel et al. (2002). The data were first published by Quillen et al. (2000).

4.2.10. *3C 338* (*Abell 2199; NGC 6166*); $z = 0.030354$

An FR I radio source in a dense environment. Two companions are prominent on the NICMOS image. The elliptical host galaxy is disturbed, with a dust lane crossing the nucleus, faintly visible in the IR. First published by Jensen et al. (2001); see also Ravindranath et al. (2001).

4.2.11. *3C 405* (*Cyg A*); $z = 0.056075$

3C 405 is the archetypal FR II radio galaxy (Carilli & Barthel 1996). There is a buried quasar detected in the host galaxy (Djorgovski et al. 1991). The hot spots are detected in the X-ray (e.g., Wilson et al. 2000). The galaxy envelope fills the $19'' \times 19''$ NIC2 chip, with the hot spots lying outside the NICMOS image. The inner galaxy contains interesting patchy and filamentary structure. There is strong dust absorption running roughly east-west below the nucleus. There is a strong patch of dust just northeast of the nucleus. There is also what looks like part of an ionization cone pointing to the northwest. At the highest brightness levels, we see a bright point source centered on a rough X shape that may define the edges of the ionization cone. Similar results have been described by Tadhunter et al. (1999).

5. HOST GALAXY MODELING RESULTS

In this section we present results for the 1D and 2D fits, a basic comparison of the results from the two techniques, and statistics describing the modeled properties of the host galaxies, for comparison to other galaxy samples.

5.1. *Ellipse Quasi-radial Profile Fits*

Properties of the ellipse fits are presented in Table 4. We note that the ellipse-fitting technique is only reliable in cases where there is no strong nuclear point source. In the presence of a strong nuclear point source, much of the galaxy structure is obscured by the asymmetric PSF, the central region of the galaxy is entirely obscured, and thus the galaxy cannot be accurately fit. In these cases, the 2D fit is able to perform far better as it can take account of the asymmetrical 2D structure of the PSF. We also note once again, that the 1D approach does not provide a true "radial profile" since adjacent elliptical isophotes will in general have different position angles and ellipticities, thus overlapping and contributing flux to each other.

5.2. *Parametric Galaxy Fits*

The direct 2D Sérsic fits are summarized in Table 5. The technique is unable to follow all of the isophotal twists in a disturbed galaxy's profile but provides an effective tool for modeling the bulk of a galaxy's flux. In addition, due to the convolution with a subpixel sampled PSF, and using the weighting scheme discussed above, we can reliably determine basic morphological parameters for even galaxies with strong quasar-like nuclei.

5.3. *Consistency*

We checked the consistency of the 1D and 2D fits by comparing the median ellipticity and position angle determined for the ellipse fits with the best-fit ellipticity and position angle in the parametric fits. For this comparison we exclude objects that have a significant nuclear point source, defined here as being one that contributes $\geq$10% of the total flux of the source. The median position angles of each source can clearly be seen to be consistent with the fitted parametric values (Fig. 4), with three outliers: 3C 129, 3C 192, and 3C 321. The ellipticities show somewhat more variation between the two modeling techniques, with 14 sources differing by >50%: 3C 79, 3C 88, 3C 105, 3C 130, 3C 135, 3C 192, 3C 264, 3C 284, 3C 319, 3C 321, 3C 338, 3C 401, 3C 438, and 3C 465. However, the Sérsic parameters obtained from the 2D parametric fit, and the 1D fit to the elliptical isophote intensities exhibit a correlation but are seen to differ significantly in many individual cases. The vast majority of objects have Sérsic indices measured in each way falling within a factor of 1.5 of each other. Three significant outliers have higher 2D Sérsic indices than 1D: 3C 88, 3C 296, and 3C 338.

Ellipse fits allow a more detailed tracing of the structure and thus have significantly better residuals than the 2D Sérsic model fits, which cannot cope with the twists in isophotes seen in many sources. Nevertheless, both techniques do a good job of modeling the bulk of the source flux in the majority of cases. We consider the 2D radial profile fits to be the "correct" approach to obtaining a meaningful radial profile. The 1D fit to elliptical isophotal data does not constitute a true radial profile due to overlapping adjacent elliptical annuli, and thus the form of the Sérsic law determined from this technique can only be an approximation. Fitting with two or three Sérsic components was attempted in several cases, and while this results in significant improvement in the fit, it is at the cost of physical interpretation of the resulting parameters. See Donzelli et al. (2007) for two-component fits to the elliptical isophotes for a large number of

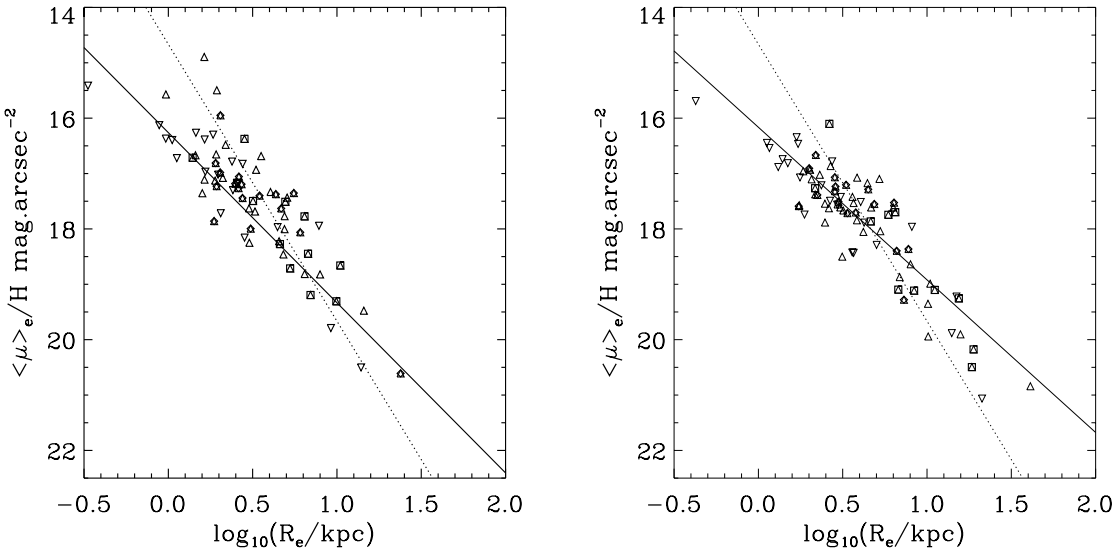

FIG. 5.—Scale-length–surface-brightness relation for the 1D (*left*) and 2D (*right*) model fits to the full sample, excluding the outliers 3C 71 and 3C 258 (not plotted; see text). Symbols are the same as in Fig. 1.

objects in the present sample. Note that the introduction of a second fitted component can drastically alter the form (Sérsic index, scale length, luminosity) of the primary modeled component. Donzelli et al. likely better model the true luminosity of the galaxy as their model provides a better overall fit to its form. However, they do not provide fits to the nuclei, and thus the quality of the Donzelli fit to the inner 1.7″ is generally poor. The present technique provides a reasonable estimate of the luminosity and form of the bulge and of the brightest nuclei and allows meaningful comparison with existing samples of quasar host galaxies and quiescent ellipticals in the literature.

If we exclude all the nuclear-dominated sources (for which one cannot trust the 1D fit results due to the asymmetric diffraction spikes dominating the ellipse-fitted isophotes) we find that the 1D and 2D fitting results are essentially identical. Indeed, in simulations where we began with simulated galaxies and progressively added stronger and stronger nuclear components and random noise, we found that the 2D approach was always able to return the original parameters of the underlying galaxy, within the errors, even once the 1D approach became unworkable due to the strength of the diffraction spikes, and resulting asymmetry in the isophotes. Furthermore, adopting only the non-nucleated sample, which one can study using *both* techniques, we find no significant change in our overall results.

5.4. *Host Galaxy Properties*

Figure 5 shows the $R_e - \mu_e$ distribution resulting from each modeling technique, excluding two outliers, 3C 71 and 3C 258. 3C 71 has an unreliable fit due to its extension across both the NIC2 and WFPC2 fields (§ 4.2.1). We believe the highly peculiar source 3C 258 to be a higher redshift quasar behind a $z = 0.165$ irregular galaxy (see § 4.1.9). Using the 2D results for the reasons discussed above, the mean effective radius, or scale length (defined throughout as the half light radius of the fitted models) for the entire sample is found to be $\langle R_e \rangle = \langle R_{1/2} \rangle = 7.46 \pm 2.00$ kpc (median = 3.63 kpc), with the mean surface within the half-light radius, $\langle \mu \rangle_e = 18.12 \pm 0.25$ mag arcsec^{-2} (median = 17.59 mag arcsec^{-2}). Quoted errors are standard errors on the mean throughout. The mean host luminosity for the sample is $\langle M_H \rangle = -23.53 \pm 0.27$ mag (median = −23.75). The mean (2D) Sérsic index for the sample is $\langle n \rangle = 3.68 \pm 0.19$ (median = 3.41), and the mean ellipticity using the same technique is $\langle 1 - b/a \rangle = 0.20 \pm 0.02$ (median = 0.18).

Excluding 3C 258 and 3C 71, we obtain the following 3 σ rejected means and standard errors for the sample:

1. $\langle R_e \rangle = 7.59 \pm 2.00$ kpc (median = 3.66 kpc).
2. $\langle \mu \rangle_e = 17.89 \pm 0.12$ mag arcsec^{-2} (median = 17.57).
3. $\langle M_H \rangle = -23.81 \pm 0.10$ mag (median = −23.77).
4. $\langle n \rangle = 3.69 \pm 0.19$ (median = 3.47).
5. $\langle 1 - b/a \rangle = 0.20 \pm 0.02$ (median = 0.18).

We now briefly consider the main subdivisions of the sample into FR I and FR II types.

5.4.1. *FR Is*

For the FR I subsample, the 3 σ rejected statistics are as follows:

1. $\langle R_e \rangle = 12.03 \pm 7.66$ kpc (median = 2.74).
2. $\langle \mu \rangle_e = 17.75 \pm 0.30$ mag arcsec^{-2} (median = 17.49).
3. $\langle M_H \rangle = -23.47 \pm 0.27$ mag (median = −23.29).
4. $\langle n \rangle = 2.77 \pm 0.31$ (median = 2.39).
5. $\langle 1 - b/a \rangle = 0.18 \pm 0.02$ (median = 0.18).

The FR I's as a class tend to have lower n ("diskier") host galaxies than the combined sample, or any other individual subsample. They account for most of the lowest-redshift ($z < 0.05$) sources, with few at higher redshifts. They exhibit a large spread in scale length, being found both in normal elliptical galaxies and in cD galaxies like 3C 84.

5.4.2. *FR II's*

For the FR II subsample the 3 σ rejected statistics are as follows:

1. $\langle R_e \rangle = 5.94 \pm 0.80$ kpc (median = 3.84).
2. $\langle \mu \rangle_e = 17.95 \pm 0.13$ mag arcsec^{-2} (median = 17.61).
3. $\langle M_H \rangle = -23.88 \pm 0.10$ mag (median = −23.84).
4. $\langle n \rangle = 3.88 \pm 0.21$ (median = 3.70).
5. $\langle 1 - b/a \rangle = 0.21 \pm 0.02$ (median = 0.19).

The FR II's represent a slightly more homogeneous population of giant "true" elliptical galaxies, with Sérsic indices close to 4. The median size is larger than that of the FR I's, and the

TABLE 6
Optical Data from the WFPC2 Archive

Source	PROPOSID	Filter	Exposure Time (s)
3C 15	6348, 5476	F555W, F702W	600, 280
3C 17	6967, 5476	F555W, F702W	600, 280
3C 20	5476	F702W	300
3C 28	5476	F702W	280
3C 29	6967, 5476	F555W, F702W	600, 280
3C 31	6673, 5476, 6673	F555W, F702W, F814W	460, 280, 460
3C 33	5156	F702W	1700
3C 33.1	6967, 5476	F555W, F702W	600, 300
3C 35	6967, 5476	F555W, F702W	600, 280
3C 52	6967, 5476	F555W, F702W	600, 280
3C 61.1	6348, 5476	F555W, F702W	600, 300
3C 66B	6673, 5476, 6673	F555W, F702W, F814W	460, 280, 460
3C 71	5754, 5754, 5754, 5479	F218W, F336W, F791W, F606W	2400, 900, 440, 500
3C 75	5476, 5927	F702W, F791W	280, 750
3C 76.1	6967	F555W	600

Notes.—Optical (WFPC2) images for each sample were obtained from the MAST (or from http://acs.pha.jhu.edu/~martel/). The table indicates the proposal ID for each image used, along with the filter for the observation and the integration time. Table 6 is available in its entirety in the electronic edition of the *Astrophysical Journal Supplement*. A portion is shown here for guidance regarding its form and content.

scale-length spread is much smaller. However, a two-sided Kolmogorov-Smirnov (K-S) test reveals little significant difference between the distributions in host luminosity or scale length. There is an 18% chance of the FR I and FR II Sérsic indices being drawn from the same distribution ($D = 0.26$).

6. COMPANIONS, JETS, MERGERS, AND INTERACTIONS

We used the SExtractor software (Bertin & Arnouts 1996) to detect and measure each candidate companion source from the `ellipse` galaxy modeling residual images. We also obtained WFPC2 optical images of all of our sources from André Martel's 3CR database (see footnote 11), or directly from the MAST (see footnote 8), most of which were previously published by de Koff et al. (1996) and Martel et al. (1999). Table 6 summarizes the origins of the optical images used in this study. We present basic companion astrometry and H-band photometry in Table 7, along with an inventory of the number of companions to each 3CR host galaxy visible on the NIC2 chip. We also manually investigated each object in the optical and the infrared, to classify each according to the presence of the following features: Shells (Malin & Carter 1983); tidal tails; mergers (clearly undergoing merger with a companion from distortion or overlapping isophotes); premergers (appear to be close to merging with a companion source); major companion sources (with infrared luminosity <1 H mag dimmer than the primary host galaxy assuming the same redshift); minor companion sources (a resolved companion source >1 H mag dimmer than the primary

TABLE 7
Companion Sources

Source	N	α (J2000.0)	δ (J2000.0)	$D/''$	H	FWHM	Elong.	Ellip.	Sh	TT	M	PM	Maj	Min	Pt	Jet	DD
3C 15	3	00 37 04.05	−01 09 05.5	16.57	19.21	8.60	1.26	0.21	...	...	...	...	...	Y	...	...	Y
3C 17	3	00 38 20.75	−02 07 41.8	6.73	22.43	7.15	2.55	0.61	...	...	...	Y	...	Y	...	...	...
3C 20	>9	00 43 09.67	+52 03 30.5	18.31	17.80	2.20	1.04	0.04	?	...	...	...	...	Y	Y	...	...
3C 28	>9	00 55 50.24	+26 24 45.5	22.65	18.84	4.31	1.04	0.04	...	...	...	...	...	Y	...	Y	...
3C 29	1	00 57 35.33	−01 23 37.4	23.63	24.04	1.98	1.47	0.32	...	...	...	...	...	...	...	...	...
3C 31	3	01 07 24.44	+32 24 44.0	15.67	21.20	2.18	1.28	0.22	...	...	...	Y	Y	...	...	Y	...
3C 33	0	...	...	...	...	...	...	...	...	Y	...	...	...	...	...	Y	...
3C 33.1	1	01 09 44.11	+73 11 54.4	4.49	17.51	4.87	1.99	0.50	...	...	...	Y	Y	...	...	...	...
3C 35	8	01 12 01.93	+49 28 44.2	15.93	17.81	2.08	1.06	0.06	...	...	...	Y	...	Y	Y	...	...
3C 52	>9	01 48 28.08	+53 32 44.8	6.60	18.66	5.12	1.40	0.29	...	...	...	...	...	Y	Y	Y	...
3C 61.1	>9	02 22 36.07	+86 19 07.7	11.73	18.10	5.47	1.12	0.10	...	Y	...	Y	Y	Y	Y	Y	...
3C 66B	4	02 23 11.54	+42 59 23.1	16.55	19.52	2.60	1.07	0.06	...	...	...	Y	Y	...	Y	...	Y
3C 71	>9	02 42 41.38	−00 00 49.4	17.70	18.06	3.23	1.13	0.11	...	...	...	...	...	Y	Y	...	...
3C 75N	4	02 57 43.63	+06 02 31.5	18.89	18.74	12.54	2.69	0.63	...	...	...	Y	Y	...	Y	...	...
3C 76.1	5	03 03 15.19	+16 26 24.2	9.65	19.99	17.36	2.24	0.55	...	Y	...	...	...	Y	Y	Y	...

Notes.—Number and properties of companion sources for each 3CR target Columns are as follows: 3CR number; number of companions on NIC2 image; coordinates of brightest companion source; distance (arcsec) of brightest companion from radio source; H-band absolute magnitude of brightest secondary; diameter (FWHM) of secondary; elongation (if resolved); ellipticity (if resolved). The right-hand side of the table lists the presence of various types of artifact (Y): shells; tidal tails; mergers; premergers; major companion sources; minor companion sources; unresolved pointlike companion sources; jets; dust disks. See the main text for a fuller description of each category. A question mark implies the presence of the artifact is suggested but cannot be confirmed categorically. Table 7 is available in its entirety in the electronic edition of the *Astrophysical Journal Supplement*. A portion is shown here for guidance regarding its form and content.

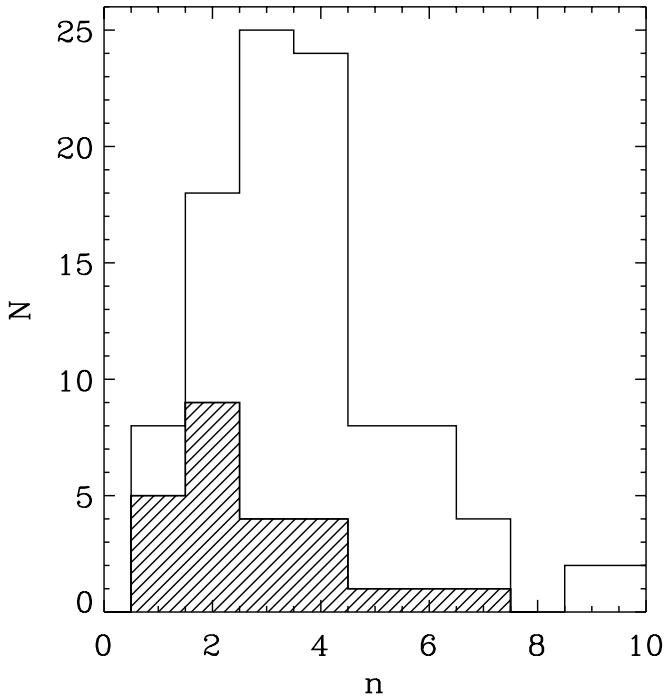

FIG. 6.—Host galaxy morphology distribution in terms of Sérsic index, n: FR I sources are shown shaded, with the solid line indicating the entire sample. The host galaxies exhibit a broader range of Sérsic n than a population of pure ellipticals, with a tail of low-n galaxies (19 at $n < 2$). These "disky" sources are listed and briefly discussed in the main text.

host galaxy assuming the same redshift); unresolved pointlike companion source (a candidate companion source that is unresolved in the NICMOS image); jets; and dust disks. The table lists the presence of each type of artifact. Below we discuss the main types encountered.

6.1. *Globular Clusters*

In the very nearest sources, the large number of detected faint, unresolved sources are likely to be globular clusters within the halo of the host galaxy. This is really only an issue in the most well-studied, nearby objects, i.e., those from archival data. In particular, 3C 71 (better known as NGC 1068) is well known for its globular cluster population. Other objects with candidate globular cluster detections are 3C 29 ($z = 0.05$); 3C 31 ($z = 0.02$); 3C 84 (Per A/NGC 1275; $z = 0.02$); 3C 88 ($z = 0.03$); and 3C 129 and 3C 129.1 (both at $z = 0.02$). At present the sample is too small, but it would be interesting from the point of view of AGN feedback models to explore whether radio jets affect the formation of globular clusters, by examining the color distributions of the globular cluster populations in these objects compared with those in quiescent ellipticals. In the merger scenario for the formation of elliptical galaxies, an older stellar population combining with a younger one produces a spread in metallicity and a bimodal distribution in the metallicity and hence color of the globular clusters (van den Bergh 2000). It is important and interesting to determine whether the globular cluster populations of radio galaxies differ from those of normal quiescent elliptical galaxies, but this lies outside the scope of the present study.

6.2. *Jets and Hotspots*

Two new optical-IR jets have been discovered by the present NICMOS imaging survey; Those of 3C 133 (Floyd et al. 2006b) and 3C 401 (Chiaberge et al. 2005). 3C 130 exhibits numerous point sources but is too distant (at $z = 0.109$) for them to be explained by globular clusters. Many of these may be hotspots, corresponding to the unusual radio morphology, and numerous hotspots observed in the radio by (Hardcastle 1998). We identify a further six sources with candidate IR-synchrotron hotspots, based on their distance, the number of unresolved sources, unusual radio morphologies and/or spatial coincidence of the unresolved sources with features on the radio map: 3C 52, 3C 61.1 (single bright unresolved source to north of galaxy), 3C 66B, 3C 219, 3C 219.1, and 3C 452.

Jets are identifiable in a further 10 sources: 3C 15 (Martel et al. 1998), 3C 66B (Butcher et al. 1980), 3C 133 (Floyd et al. 2006b), 3C 264 (Crane et al. 1993), 3C 274 (Curtis 1917), 3C 277.3 (Miley et al. 1981), 3C 293 (Floyd et al. 2006a), 3C 346 (Dey & van Breugel 1994), 3C 371 (Nilsson et al. 1997), and 3C 401 (Chiaberge et al. 2005). Extended emission line regions with the appearance of jets are clearly visible in 3C 171 and 3C 234.

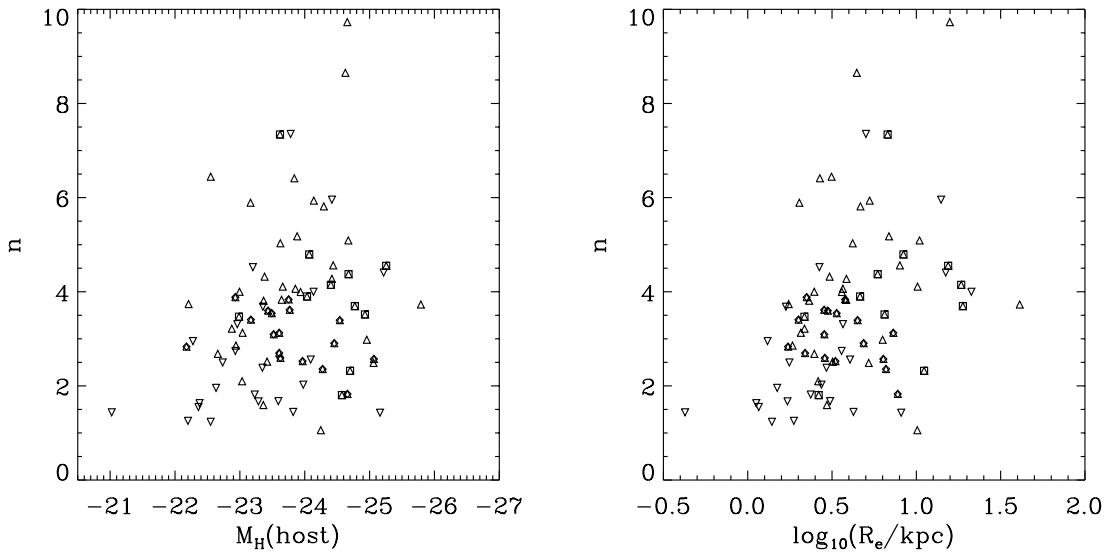

FIG. 7.—Weak correlations are observed between the Sérsic index, n, and the host galaxies' luminosity and scale length. Powerful radio galaxies can only be hosted by disk-dominated galaxies if the galaxy is exceptionally massive. Symbols are the same as in Fig. 1.

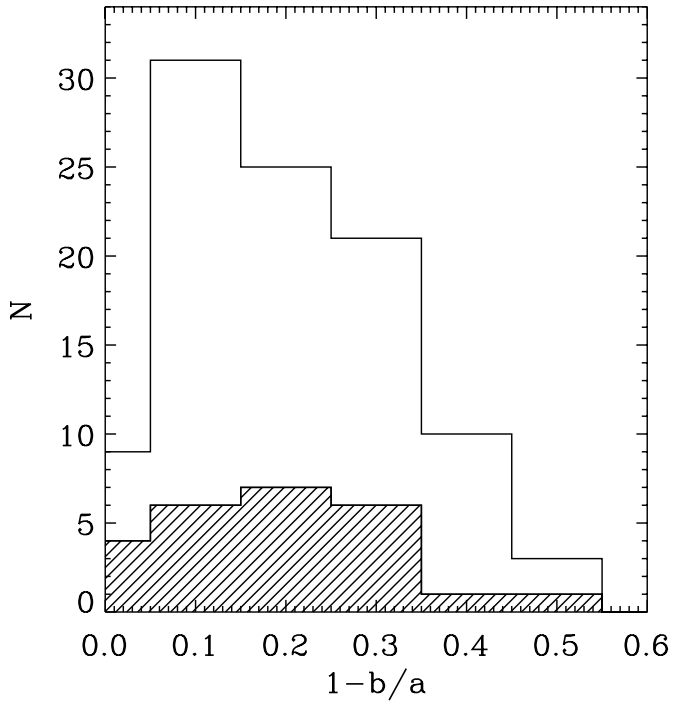

FIG. 8.— Ellipticity distribution for the full sample (*unshaded*) and for the FR I's (*shaded*).

6.3. *Dust Disks*

Thirty-one objects in the sample are seen to possess ~100 pc scale distributions of dust and gas in their nuclear regions, often in settled, disklike structures surrounding the AGNs. See Tremblay et al. (2007) for further details. Eleven of these are FR I sources; 16 are identified as FR II's.

6.4. *Mergers and Premerger Candidates*

Six sources are clearly identifiable as mergers through their overlapping isophotes and disturbed appearance: 3C 79, 3C 293 (Floyd et al. 2006b), 3C 321, 3C 346, 3C 405, and 3C 433. There are an additional 28 sources that qualify as "premergers," or candidate mergers that cannot be confirmed by the overlapping of isophotes of the two partners. "Major" secondary sources are identifiable in 20 sources (20%). Minor secondaries are identified in 55 sources, or 56% of the sample. Fifty-nine sources have unresolved companions. A number of these may turn out to be foreground stars, especially for sources at low Galactic latitudes, but it seems unlikely that all such sources are so explained. For a small number we also obtain detections in the optical, and these sources typically have colors of $R - H = 2$–3. The exact nature and redshifts of these sources must await a detailed spectroscopic study, which could confirm whether the candidate companions indeed lie at the same redshift as the radio source and further identify the stellar makeup of the sources. However, based on the sheer number of small companions, we conclude that these are of significant importance to the 3CR sample and to the radio source phenomenon itself. The broadband colors of many of these sources are consistent with an old stellar population, perhaps the stripped core of a late-type spiral or compact early-type galaxy that has undergone merger with the main galaxy, losing its gas and dust to the more massive system. Such a mechanism would provide a natural means to fuel the AGN activity. As far as we are aware, this is the first such detection in large numbers of sources across a range in redshifts. Examples of dwarf ellipticals and of globular clusters have been observed in a number of nearby sources, e.g., Fornax.

7. DISCUSSION

7.1. *Galaxy Morphologies*

We find a broad distribution of Sérsic indices in our sample, spanning the full range from $n = 1$ (exponential disks) to $n = 4$ (de Vaucouleurs ellipticals) and higher (see Fig. 6). There is a moderately strong correlation (Spearman's rank $\rho = 0.42,\ p = 1.7 \times 10^{-5}$) between scale length and Sérsic n (see Fig. 7). Interestingly, neither the FR I's nor the FR II's considered alone show such a significant correlation (FR I: $\rho = 0.56,\ p = 0.0055$; FR II: $\rho = 0.35,\ p = 0.0078 \times 10^{-3}$). There is a somewhat weaker anticorrelation between the host galaxy absolute magnitude and the Sérsic index, n ($\rho = -0.32,\ p = 0.001$)—once again, somewhat weaker in the individual subsamples. Thus, the larger, more luminous galaxies tend to be more "bulgy." The Sérsic index is also found to correlate weakly with redshift ($\rho = 0.28;\ p = 0.006$). Thus, the disky sources tend to be lower redshift, and lower IR luminosity, but interestingly, no strong relationship is found between Sérsic index and radio power (either core or total). However, there are very few sources that have Sérsic indices $n < 2$, thus this is not an indication that true "disk" galaxies are capable of hosting powerful radio sources. Rather, it indicates that within the radio source population, there

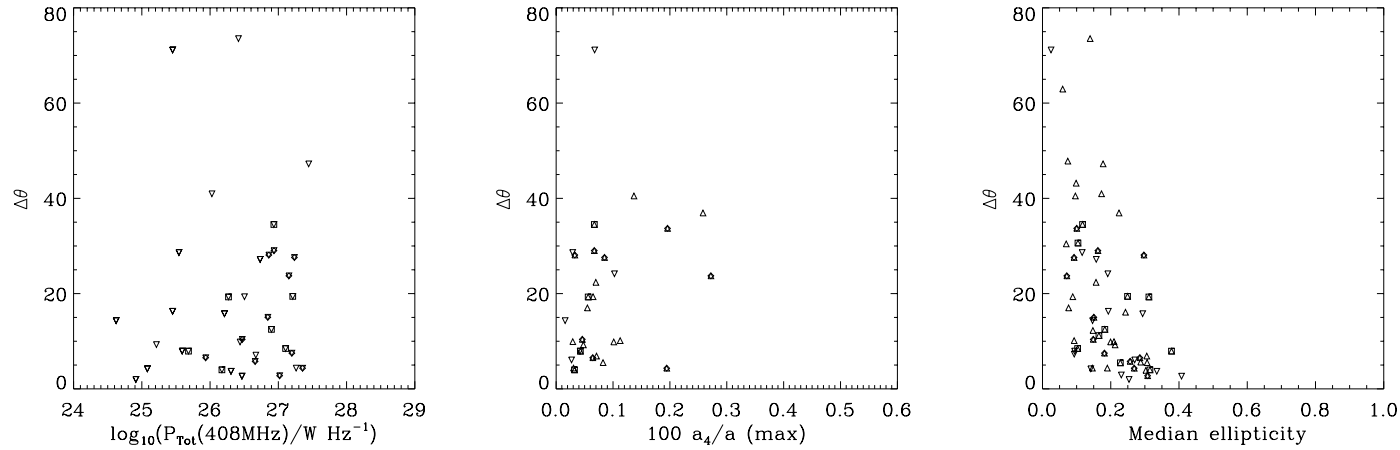

FIG. 9.— Isophotal twist angle, $\Delta\theta$ against (*left to right*): total radio power, boxiness (a_4), and median ellipticity. Rounder galaxies tend to have larger isophotal twists, and, as found by Gopal-Krishna et al. (2003), radio galaxies exhibit a correlation between twist angle and total radio power. Symbols are the same as in Fig. 1.

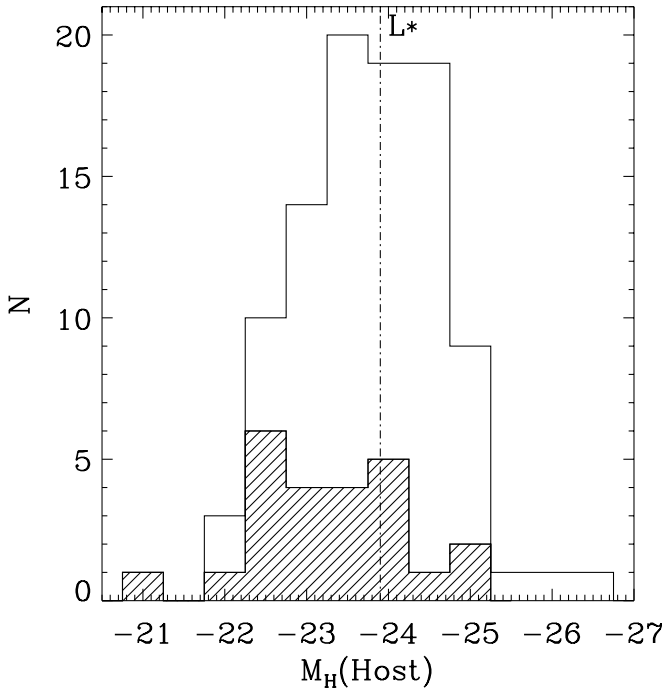

FIG. 10.—Galaxy luminosity distribution for the full sample (*unshaded*) and for the FR I's (*shaded*): 3CR sources generally hosted by super-L^* objects. The low-luminosity tail is dominated by low-redshift ($z < 0.09$) and FR I targets.

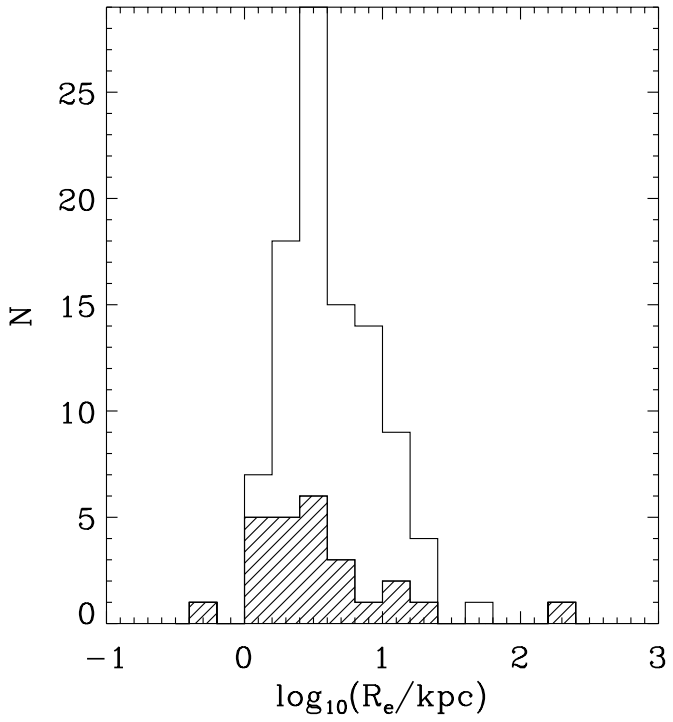

FIG. 11.—Scale-length distribution for the full sample (*unshaded*) and for the FR I's (*shaded*).

is a strong requirement for an elliptical, or bulge-dominated host galaxy, and a strong dependence of radio luminosity on host galaxy size and luminosity, but not on Sérsic index within the range $2 < n < 10$. A more "bulgy" bulge does not allow for a more powerful radio source, while a more luminous bulge does.

There are a number of exceptions to the general rule; 17 of the host galaxies have $n < 2$ and would thus be classed as disky. Ten of these sources are low-redshift ($z < 0.05$), nine of those being FR I low-power radio sources. However, there are eight FR II sources, and five of these are at $z > 0.1$: 3C 173.1, 3C 234, 3C 288, 3C 323.1, and 3C 332. All five of these FR II sources have close companion objects and are either merging or are likely to be postmerger systems. They generally show evidence of dusty environments from their optical and IR images, except for 3C 323.1, which has a quasar-like nucleus in both the optical and IR.

7.1.1. *Ellipticity*

The 3CR host galaxies are slightly rounder, on average, than the general elliptical galaxy population, with a sharp peak at E1, and no objects more eccentric than E5. See Figure 8.

7.1.2. *Isophotal Twists*

The total isophotal twist angle, $\Delta\theta$, was computed for each galaxy from the position angle profile. We neglect the inner $0.5''$, and neglect $>1\,\sigma$ outliers in the θ profile. We then quantify the twist in terms of the total position angle variation of the major axis over the entire range in surface brightness (after Gopal-Krishna et al. 2003). Objects that are less elliptical than $1 - b/a < 0.2$ over their entire range are also discounted; as for these extremely round objects, a spuriously large twist angle can arise due to the circular symmetry of the isophotes. The resulting twist angles are plotted in Figure 9. We confirm that the trend between total radio power and twist angle first noted by Gopal-Krishna et al. (2003) for the radio galaxy sample of Govoni et al. (2000) is also seen in the present sample.

7.2. *Galaxy Luminosities and Scale Lengths*

The host galaxy luminosity distribution is shown in Figure 10, with their scale length distribution shown in Figure 11. All of the 3CR sources studied, except for 3C 258, 3C 270, and 3C 296, are hosted by galaxies with luminosities above $M_H = -22$, and scale lengths >1 kpc. The highly peculiar and disturbed 3C 258 (see earlier comment in § 4.1.9) is found to have an extremely

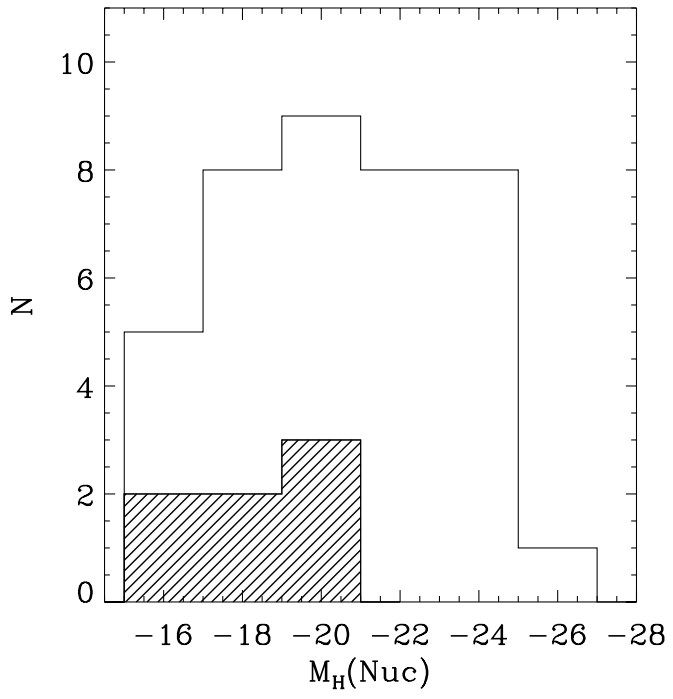

FIG. 12.—Nuclear luminosity distribution for the full sample (*unshaded*) and for the FR I's (*shaded*): We have detected unresolved IR nuclei in 39 objects, down to an absolute H-band magnitude of -15.

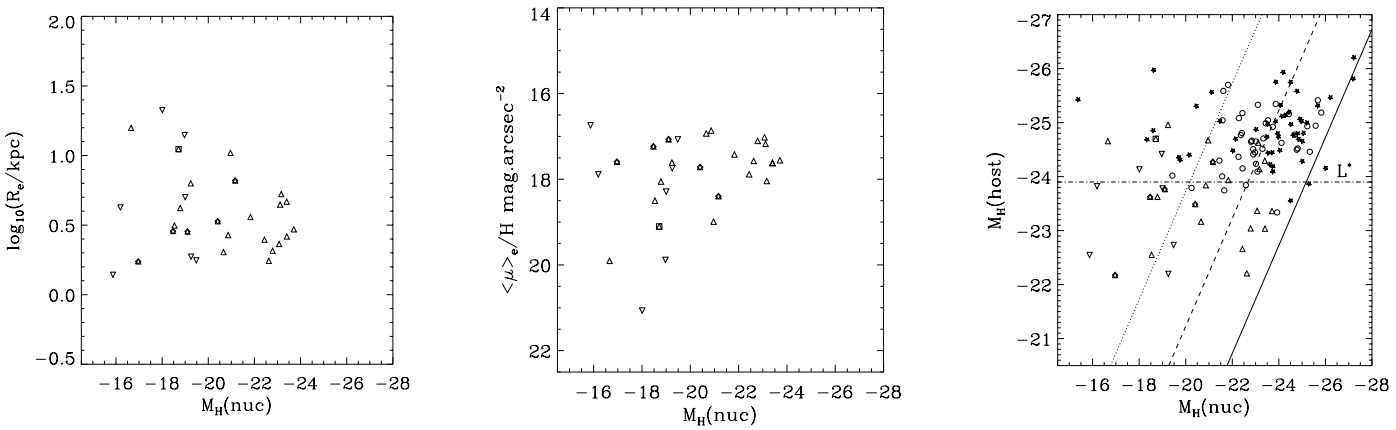

FIG. 13.—Nuclear IR luminosity vs. host galaxy properties, *left to right*: Scale-length, surface brightness, and host galaxy luminosity. There is a slight tendency for stronger nuclear sources to be located in higher surface-brightness galaxies. No trend is observed between nuclear luminosity and host luminosity (*right*) or scale length (*left*).

compact and low-luminosity host galaxy, consistent with it being at a much higher redshift.

Half of the sources have host galaxies brighter than $L^{\star}$, and larger than 3 kpc, with the peak in the luminosity and scale-length distributions just below $L^{\star}$ and 3 kpc, respectively. This is as to be expected based on our knowledge of radio galaxies (e.g., Zibetti et al. 2002), quasar host galaxies (Dunlop et al. 2003; Floyd et al. 2004), and unification schemes (Barthel 1989): Our understanding of the AGN phenomenon hinges on the presence of a supermassive black hole as the ultimate energy source, and our growing demographic understanding of galaxies is that a massive black hole requires a massive galaxy bulge or spheroid to host it.

The low-luminosity tail of the sample is dominated by low-redshift and low-radio-power FR I's. Of the 22 sources with luminosities $M_H > -23$, 19 are at $z < 0.09$, with only 3C 61.1, 3C 258 (once again), and 3C 314.1 breaking the general rule.

3C 61.1 at $z = 0.186$ has an unusual radio morphology and appears to be hosted by an unusually faint, small galaxy at the center of a small group. The optical image shows complex structure (de Koff et al. 1996), with tails of emission that resemble spiral arms, and which do not correlate with the radio emission features (Leahy & Perley 1991). However, the published 20 cm VLA radio map is of low resolution, and it is difficult to confirm the location of the optical-IR counterpart accurately.

3C 314.1 has an unusually low-surface-brightness host galaxy at $z = 0.119$, with a slightly dusty appearance from the optical-IR images.

7.3. *Infrared Nuclei*

A number of our sources (40%) have clearly detectable infrared nuclear activity. We were able to detect nuclear point sources down to an absolute magnitude of $M_H(\mathrm{Nuc}) = -15$ (Table 5 and Fig. 12). A more exhaustive search for faint nuclei and a discussion of their origin will be the subject of another paper (M. Chiaberge et al. 2008, in preparation). First, we note that nuclear point sources are detected in *both* FR I's and FR II's, with roughly equal probability within our sample (38% of FR I's, 41% of FR II's). No significant correlation is found between the NIR nuclear luminosities of the sources in which we have identified unresolved nuclear point sources, and the host luminosity, nor scale length, although a weak correlation is seen with host galaxy surface brightness ($\rho = 0.34$; $p = 0.035$; see Fig. 13). The difference in the luminosity range of FR I and FR II sources is very clearly seen from Figure 12: FR I's, although they can possess nuclei, do not contain the luminous quasar-like nuclei that are seen in the FR II population.

7.4. *Kormendy Relation* (R-μ)

The strong correlation between scale length and surface brightness is a well-known feature of elliptical galaxies (Kormendy 1977). The relation followed by the present low-redshift 3CR sample is somewhat lower than that of 3.33 ± 0.09 established for early-type galaxies using the Sloan Digital Sky Survey (Bernardi et al. 2003), following a slope of 3.0 ± 0.1:

$$\mu_{3\mathrm{CR}} = 16.0 \pm 0.1 + (3.0 \pm 0.1)\log(R_e).$$

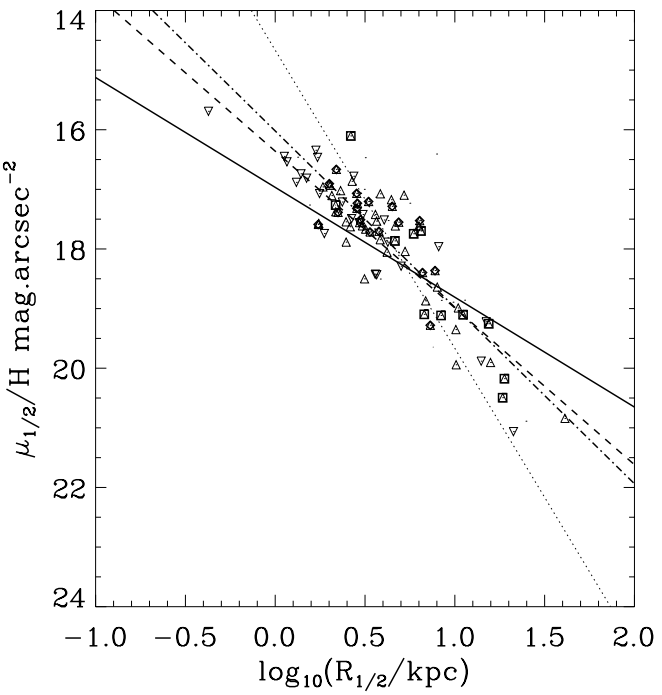

FIG. 14.—Best-fitting scale-length–surface-brightness relation for the full sample (*solid line*), the FR I's (*dashed line*), and the FR II's (*dot-dashed line*). The locus of an $L^{\star}$ galaxy is shown by the dotted line.

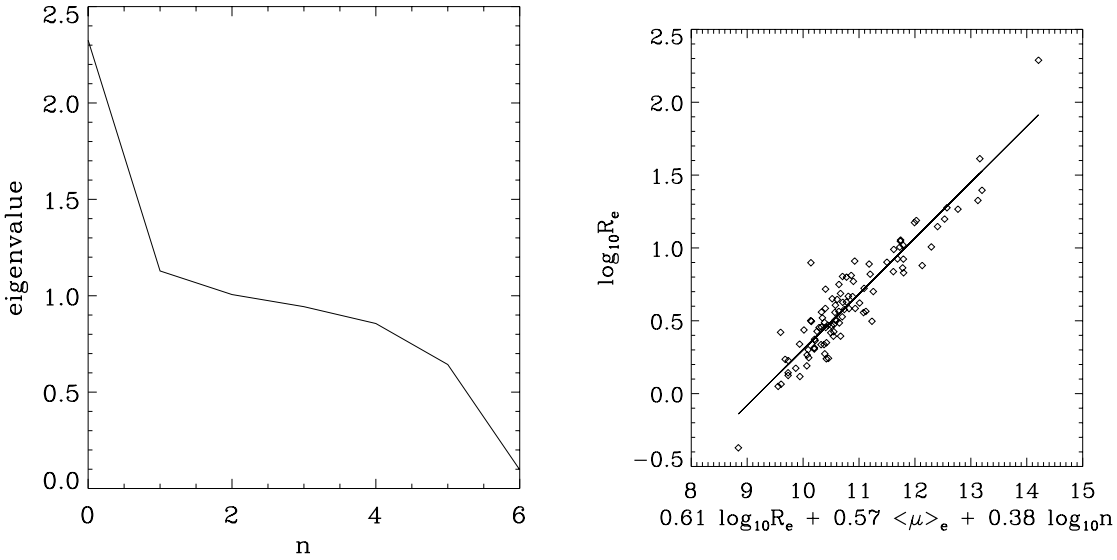

FIG. 15.—*Left*: Eigenvalues from the principal component analysis on the fitted parameters from the 2D (Galfit) modeling. Only the first eigenvector accounts for a significant proportion of the scatter in the entire data set. *Right*: Photometric fundamental plane (eigenvector 1).

Kormendy fits to the FR I's and FR II's yield somewhat different slopes of 3.46 ± 0.1 and 2.67 ± 0.1, respectively (Fig. 14):

$$\mu_{\rm FR\ I} = 15.9 \pm 0.1 + (3.46 \pm 0.1)\log(R_e),$$

$$\mu_{\rm FR\ II} = 16.1 \pm 0.1 + (2.67 \pm 0.1)\log(R_e).$$

7.5. *Fundamental Plane*

We used principal component analysis (PCA) to explore the model parameter space for any three-dimensional correlations, like the photometric "fundamental plane" reported for normal elliptical galaxies by Khosroshahi et al. (2000b, 2000a). PCA looks for correlations among a set of multidimensional data and rotates the coordinate axes from being aligned with the input parameters to new directions that are aligned with the directions of greatest variance of the data—the principal axes. In order to prevent the choice of units from artificially weighting some parameters more than others, each parameter is first normalized by subtracting its mean and dividing by its variance. The PCA is then performed on these normalized variables. In the output, each of the eigenvectors—the principal axes—is written as a linear combination of the original (but normalized) parameters. The eigenvalues are scaled so that the sum of all eigenvalues equals the total number of eigenvectors (and therefore the total number of parameters as well). In Figure 15 we show the "scree plot" of eigenvalues associated with the seven eigenvectors fit, along with a plot of the data over the first eigenvector. Only the first eigenvector accounts for a significant quantity of the scatter in the parameter space, and is made up almost entirely of R_e, μ_e, and Sérsic n. The recovered form of the relationship is

$$R_e \propto I_e^{-0.72} n^{0.20}.$$

7.6. *Host Galaxy Colors*

For the cross-sample of this paper and Martel et al. (1999) we can produce accurate $R - H$ colors for the host galaxy, shown in Table 8. A color–absolute magnitude diagram for this subsample is presented in Figure 16. An extremely steep trend is seen between color of the host galaxy ($R - H$) and absolute H-band magnitude of the host galaxy, with a slope of roughly 1. The extremely red colors at the top end of the sequence are likely due to dust absorption in the optical images of sources like 3C 293, 3C 296, 3C 388, and 3C 403. The blue outliers are all nucleated sources, in which the Martel et al. fluxes are likely to be higher than the true galaxy flux, as no attempt was made by those authors to separate host and nucleus.

7.7. *Host Galaxy Masses*

Based on the apparent similarity between the present sample, and the normal quiescent elliptical galaxy population, we have applied the finding of Zibetti et al. (2002) that H-band

TABLE 8
HOST GALAXY $R - H$ COLORS

Source	R[a]	H	$R - H$
3C 15	16.84	13.55	3.29
3C 29	16.53	12.89	3.64
3C 31	13.78	11.18	2.60
3C 35	16.84	13.68	3.16
3C 66B	14.38	11.72	2.66
3C 75N	14.22	12.07	2.15
3C 83.1	13.92	11.53	2.39
3C 84	13.50	12.45	1.05
3C 88	15.92	12.23	3.68
3C 98	15.26	13.03	2.23
3C 111	17.12	14.83	2.29
3C 198	17.64	15.58	2.06
3C 227	16.21	15.61	0.60
3C 236	17.62	14.54	3.08
3C 264	14.17	12.55	1.62

NOTE.—Approximate $R - H$ colors for the sources based on R-band fluxes at a 20 kpc aperture. Table 8 is available in its entirety in the electronic edition of the *Astrophysical Journal Supplement*. A portion is shown here for guidance regarding its form and content.

[a] Martel et al. (1999).

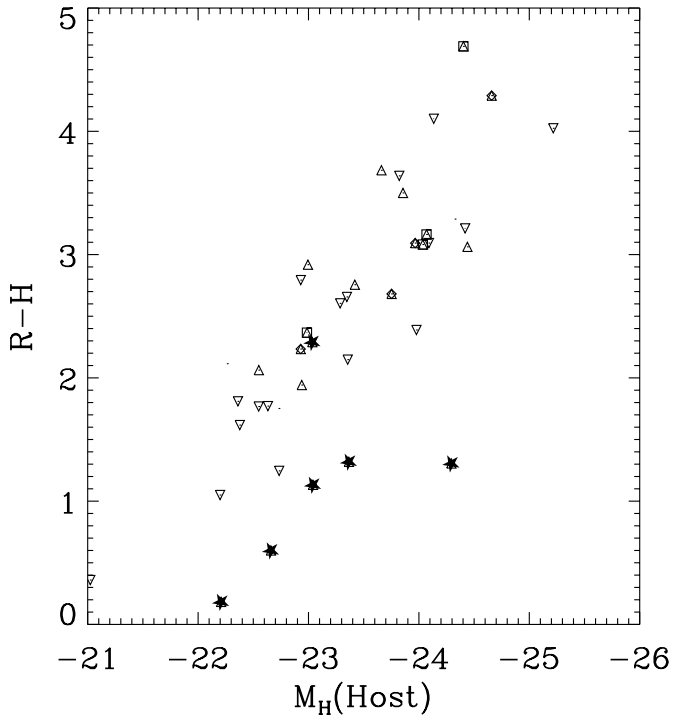

FIG. 16.—Color–absolute magnitude diagram for the sample. More luminous hosts are significantly redder. Nucleated sources (with nuclei brighter than $M_H = -21$) are shown by a filled star, and dominate the blue end off the distribution.

luminosity provides a first order estimate of the dynamical mass of an elliptical galaxy. They find a mean mass-to-light ratio of $\log(M/L_H) = 0.09$ (in solar units) that is independent of total luminosity. There is an approximately 0.2 dex 1 σ scatter on this relationship. The mean mass of a 3CR host galaxy from the present sample is $2 \times 10^{11}\ M_\odot$, but with very large scatter, in particular due to the two enormous outliers, 3C 130 ($10^{12}\ M_\odot$) and 3C 338 ($5 \times 10^{12}\ M_\odot$). Clearly, the assumption of constancy of the mass-to-light ratio for our sample needs verification by dynamical means, and we would argue that a significant hole in the current 3C literature is a fundamental plane relationship (R-μ-σ) study to test whether these objects truly are dynamically representative of normal elliptical galaxies. In the absence of long-slit spectra in the public domain, such a work is currently nonexistent.

8. SUMMARY AND CONCLUSIONS

Ellipse and Galfit models have been presented for 101 $z < 0.3$ 3CR radio source host galaxies. The two fitting methods (1D and 2D) are found to be statistically consistent for nonnucleated sources, although individual sources can provide significantly differing results using the two methods. Simulations have revealed that, with the addition of an artificial nuclear point source to a real source, we are still able to obtain accurate results using the 2D technique, after the 1D technique has failed.

Unresolved nuclear point sources are detected with equal likelihood down to $M_H = -15$ in both FR I and FR II galaxies. FR I's can have faint unresolved nuclei (all dimmer than $M_H = -20$), but these mostly exist in low-redshift sources in this radio-flux–limited sample. We find no significant difference in properties of the host galaxies between nucleated and nonnucleated sources.

The host galaxies of the 3CR are generally consistent with the elliptical galaxy population: They exhibit a Kormendy relation that is similar to that of quiescent ellipticals and quasar host galaxies; the peak in the host galaxy luminosity distribution is close to $L^\star$, with steeper dropoff to high luminosity than low; there is a strong correlation between host H-band luminosity and $(R - H)$ color. However, the 3CR exhibit a large spread in Sérsic index to low values, and include a number of quite disky sources. Sérsic n is not found to correlate with the radio luminosity, and yet the disky (low-n) wing of the sample is dominated by low-z, low radio-power sources, merging sources, and sources with luminous companions. This suggests that disky galaxies are capable of hosting powerful radio sources, providing that they are massive enough or are undergoing a major merger.

Approximately 50% of our sample exhibit compact, often unresolved, companion sources that are too red and faint to have been detected in previous optical snapshot programs. Spectroscopy is required to determine the nature and redshifts of these sources. Their typical colors (where this can be determined) are around $R - H = 2$–3, consistent with mature stellar populations at the redshift of the primary source. These sources are found predominantly in elliptical host galaxies and have three likely origins: foreground stars—likely in cases with low Galactic latitude; synchrotron hotspots—particularly in a few peculiar radio sources; merger remnants—compact cores from cannibalized small galaxies (e.g., Canalizo et al. 2003); or molecular gas clouds infalling into the galaxy (Bellamy & Tadhunter 2004). By comparison, only $\sim$10% of our sample show signs of an ongoing or recent major merger, typical of the elliptical galaxy population in general (although many more show other signs of disturbance). If many of these sources do turn out to be galactic nuclei, it would suggest that a minor merger is sufficient to fuel or refuel a quiescent black hole in an elliptical galaxy into radio-loud AGN activity, while disky galaxies appear to require a more major disturbance. There is a correlation between radio power and the isophotal twist angle within our sample with all sources exhibiting significant isophotal twists. We thus conclude that, while bulgy elliptical galaxies host the majority of powerful radio sources, it is possible to trigger such activity in diskier objects through mergers. The diskiness may simply be a morphological distortion resulting from the merger, or the merger may be able to provide sufficient fuel to a black hole in a disky galaxy to trigger behavior only normally seen in the more massive black holes at the centers of ellipticals.

A detailed spectroscopic study of the 3CR host galaxies is overdue. It is important to explore the dynamical states of these objects to place them on the "fundamental plane" (R-μ-σ) of galaxies. The nature of the companion sources needs to be explored, ideally using imaging spectroscopy to determine their redshifts and compositions at the same time as exploring the makeup of the 3CR host galaxy itself.

Based on observations with the NASA/ESA *Hubble Space Telescope*, obtained at the Space Telescope Science Institute, which is operated by the Association of Universities for Research in Astronomy, Inc. (AURA), under NASA contract NAS5-26555. We gratefully acknowledge support from *HST* grant STGO-10173. We wish to thank the anonymous referee for constructive comments and suggestions that significantly improved the reading of this paper.

APPENDIX

CONSISTENCY OF GALFIT AND 2DM

In this paper we have used Galfit (Peng et al. 2002) to perform 2D modeling of the host galaxies of the 3CR. But we have adopted the error treatment of 2DM (McLure et al. 1999; Floyd et al. 2004) in cases in which the nucleus dominates (i.e., provides $\gtrsim$1/2 of the total flux). In this section we explore the consistency of the two approaches in a series of test cases using both real and simulated galaxies.

2DM was designed for use on QSO host galaxies and is a simpler fitting code than Galfit. The major difference is in assignment of errors, as for the PSF-dominated cores of QSO images it is the PSF sampling error that dominates any fitted model, and the Poissonian error on the flux in a given pixel is an insufficient determination of the error in the model fit (Floyd et al. 2004). In its standard form it fits a single Sérsic host galaxy component and a nuclear component, centered at the same fixed position.

Galfit and 2DM were used to model the host galaxy flux of three radio galaxies from the sample: 3C 66B, 3C 111, and 3C 449. These three were specifically chosen to span the range of infrared nuclear activity seen across the sample: 3C 449 shows no sign of an unresolved nuclear point source, while 3C 66B shows a weak pointlike nucleus, and 3C 111 is a quasar. All data have been reduced following the technique described in § 2. We have modeled each object using a single Sérsic component model in Galfit, as described in § 3, and using 2DM as described in Floyd et al. (2004). The resulting models are presented in Table 9. Next, synthetic galaxies were constructed *based on the parameters recovered from these three objects*, using Galfit. Random noise was added to each synthesized test case at incrementing levels, and these noisy synthetic targets are then remodeled with Galfit and 2DM to explore the stability of fit to noise and ability to recover the "true" properties of the host galaxy. The results of this test are explored in § A2 below.

A1. MODELS OF THE THREE REAL TEST CASES

The best-fit model parameters for the three objects, 3C 66B, 3C 111, and 3C 449, using each of the modeling techniques, are presented side by side for comparison in Table 9. Radial profiles are shown in Figure 17. 2DM and Galfit are clearly seen from the table to be in good agreement. The host fluxes generally agree well (to within $\sim$2%) and the scale lengths within $\sim$10%. However, in the case of the quasar, 3C 111, there is a larger discrepancy, and greater dependence on the treatment of errors in the central region. There is also a significant discrepancy in the value of the nuclear flux in all three sources. This is once again, very dependent on the error treatment.

A2. SYNTHETIC GALAXY TESTS

We constructed simple synthetic galaxy models using Galfit (in nonoptimization mode) and the parameters recovered from the three real test cases (3C 66B, 3C 111, 3C 449). To these idealized galaxy models, varying amounts of noise were added, and different PSFs convolved with the data, in order to produce a synthetic NICMOS observation of an idealized galaxy. These synthetic observations were then modeled using 2DM. We began with the simplest case of the original models convolved with the PSFs, with no noise or background added. 2DM was then run just once to see how reliably it could recover the original parameter set used to define the synthetic observation. Results are presented for this "quick" run in Table 10. 2DM is found to recover the properties of the Galfit models to within $\sim$10%. Note that in normal use, 2DM is run repeatedly to refine these fitting results. However, we adopt 10% as a reasonable estimate for the systematic errors inherent in fitting nonideal galaxies with idealized forms.

TABLE 9
GALFIT/2DM RESULTS: REAL TEST-CASE GALAXIES

Code	Mag(host)	R_e/kpc	$n(=1/\beta)$	b/a	θ	Mag(nuc)
			3C 66b			
Galfit	12.47	2.93	1.64	0.92	−79.4	19.40
2DM(nosamp)	12.52	2.67	1.55	0.91	−86.5	19.29
2DM(samp)	12.47	2.81	1.67	0.91	−85.9	18.64
			3C 111			
Galfit	14.40	2.26	6.98	0.72	16.8	15.05
2DM(nosamp)	14.58	2.24	4.28	0.63	17.4	15.04
2DM(samp)	14.71	2.95	3.75	0.63	17.2	14.71
			3C 449			
Galfit	12.48	1.90	1.36	0.84	−6.4	21.34
2DM(nosamp)	12.51	1.81	1.30	0.86	−7.7	20.46
2DM(samp)	12.49	1.84	1.37	0.85	−7.2	20.52

NOTES.—Comparison of results of fitting the three test case objects with Galfit and 2DM. Position angles are in degrees counterclockwise from north. All magnitudes are uncorrected AB magnitudes from the PHOTFNU header keyword. Scale-lengths are half-light radii on the semimajor axis. The center of the galaxy and nucleus are fixed at the same position in Galfit as in 2DM, in order to force a comparison based on the same number of parameters. For 3C 111 this posed problems (see text), so we present the Galfit models both with and without a fixed center.

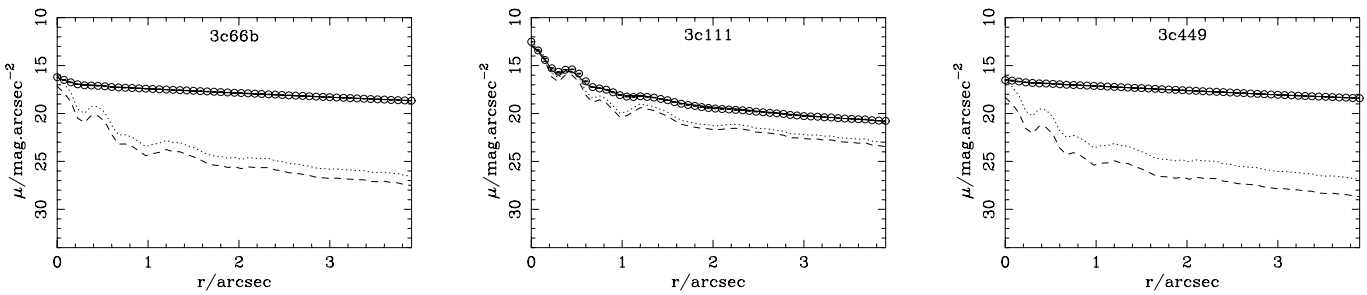

FIG. 17.— 2DM radial profiles for the three test cases. Solid lines indicate best-fit 2DM model. Dashed lines indicate the best-fit nuclear component, with the dotted lines indicating the PSF scaled to match the nuclear flux of the source.

TABLE 10
GALFIT/2DM RESULTS: SYNTHETIC GALAXIES

Code	Mag(host)	R_e/kpc	$n(=1/\beta)$	b/a	θ	Mag(nuc)
A (Simulated 3C 66B)						
Galfit	12.47	2.93	1.64	0.92	-79.4	19.40
2DM	12.38	3.15	1.89	0.90	-72.4	19.87
B (Simulated 3C 111)						
Galfit	14.40	2.26	6.98	0.72	16.8	15.05
2DM	14.56	2.15	3.64	0.74	13.5	15.34
C (Simulated 3C 449)						
Galfit	12.48	1.90	1.36	0.84	-6.4	21.34
2DM	12.49	1.87	1.34	0.84	-6.3	21.22

NOTES.— Comparison of results of fitting the three synthetic galaxies, constructed with Galfit using the parameters deduced for the three real test cases. Galfit recovers the parameter values to within 10% in a single run (no added noise).

TABLE 11
RESPONSE OF GALFIT TO SYNTHETIC GALAXIES PLUS NOISE

Galaxy	Mag(host)	R_e/kpc	$n(=1/\beta)$	b/a	θ	Mag(nuc)
A (Simulated 3C 66b)						
Original	12.47	2.93	1.64	0.92	-79.4	19.40
Recovered($1e^-$ Poisson)	12.47	2.93	1.64	0.92	-79.4	19.40
Recovered($10e^-$ Poisson)	12.47	2.93	1.64	0.92	-79.4	19.41
B (Simulated 3C 111)						
Original	14.40	2.26	6.98	0.72	16.8	15.05
Recovered ($1e^-$ + Poisson)	14.40	2.26	6.93	0.72	16.8	15.05
Recovered ($10e^-$ + Poisson)	14.39	2.26	7.01	0.72	16.8	15.06
C (Simulated 3C 449)						
Original	12.48	1.90	1.36	0.84	-6.4	21.34
Recovered ($1e^-$ + Poisson)	12.48	1.89	1.36	0.84	-6.4	21.32
Recovered ($10e^-$ + Poisson)	12.48	1.89	1.36	0.84	-6.4	21.33

NOTES.—Galfit results for fits to three synthetic test case galaxies constructed with varying degrees of read noise (1 and 10 e^-) plus Poisson noise. The three test cases are based on the Galfit models for 3C 66B, 3C 111, and 3C 449. The top line of each row gives the true parameters for the synthetic galaxy. The subsequent rows show the results recovered by running Galfit . Each run was initiated at a generic starting point, not tailored to the individual cases.

Next we added in an additional random "read noise" component to the simulated galaxies and reran the Galfit minimization, starting from a generic starting point, as described in Floyd et al. (2004). Recovered parameters are presented in Table 11. The parameters are recovered almost perfectly from each galaxy with read noise of 1–10 e^-, plus Poisson.

A3. WORKING CONCLUSIONS

The results from 2DM and Galfit agree typically to within ∼10% on morphological parameters, ∼2% on host flux. However, there is a degree of variation, depending in particular on the treatment of errors in the central regions. This is in part due to the different convolution algorithms applied. For highly luminous objects this leads to a disagreement in some host properties, while for all sources, there is still a large margin of error in the nuclear luminosity.

REFERENCES

Akujor, C. E., Spencer, R. E., Zhang, F. J., Davis, R. J., Browne, I. W. A., & Fanti, C. 1991, MNRAS, 250, 215
Antonucci, R. R. J., & Miller, J. S. 1985, ApJ, 297, 621
Bahcall, J. N., Kirhakos, S., Saxe, D. H., & Schneider, D. P. 1997, ApJ, 479, 642
Barthel, P. D. 1989, ApJ, 336, 606
Baum, S. A., et al. 1997, ApJ, 483, 178
Bellamy, M. J., & Tadhunter, C. N. 2004, MNRAS, 353, 105
Bender, R., Burstein, D., & Faber, S. M. 1992, ApJ, 399, 462
Bennett, A. S. 1962, MmRAS, 68, 163
Bernardi, M., et al. 2003, AJ, 125, 1849
Bertin, E., & Arnouts, S. 1996, A&AS, 117, 393
Best, P. N., Kaiser, C. R., Heckman, T. M., & Kauffmann, G. 2006, MNRAS, 368, L67
Bower, G. A., et al. 2000, ApJ, 534, 189
Butcher, H. R., van Breugel, W., & Miley, G. K. 1980, ApJ, 235, 749
Canalizo, G., Max, C., Whysong, D., Antonucci, R., & Dahm, S. E. 2003, ApJ, 597, 823
Canalizo, G., & Stockton, A. 1997, ApJ, 480, L5
Caon, N., Capaccioli, M., & D'Onofrio, M. 1993, MNRAS, 265, 1013
Capetti, A., de Ruiter, H. R., Fanti, R., Morganti, R., Parma, P., & Ulrich, M.-H. 2000a, A&A, 362, 871
Capetti, A., Trussoni, E., Celotti, A., Feretti, L., & Chiaberge, M. 2000b, MNRAS, 318, 493
Carilli, C. L., & Barthel, P. D. 1996, A&A Rev., 7, 1
Cattaneo, A., Dekel, A., Devriendt, J., Guiderdoni, B., & Blaizot, J. 2006, MNRAS, 370, 1651
Chiaberge, M., et al. 2005, ApJ, 629, 100
Corbin, M. R., O'Neil, E., & Rieke, M. J. 2002, AJ, 124, 183
Crane, P., et al. 1993, ApJ, 402, L37
Croton, D. J., et al. 2006, MNRAS, 365, 11
Curtis, H. 1917, PASP, 29, 177
de Koff, S., et al. 1996, ApJS, 107, 621
Dey, A. 1994, Ph.D. thesis, Univ. California, Berkeley
Dey, A., & van Breugel, W. J. M. 1994, AJ, 107, 1977
Di Matteo, T., Springel, V., & Hernquist, L. 2005, Nature, 433, 604
Djorgovski, S., Weir, N., Matthews, K., & Graham, J. R. 1991, ApJ, 372, L67
Donzelli, C., Chiaberge, M., Macchetto, F. D., Madrid, J. P., Capetti, A., & Marchesini, D. 2007, ApJ, 667, 780
Dunlop, J. S., McLure, R. J., Kukula, M. J., Baum, S. A., O'Dea, C. P., & Hughes, D. H. 2003, MNRAS, 340, 1095
Faber, S. M., et al. 1997, AJ, 114, 1771
Fanti, C., Fanti, R., de Ruiter, H. R., & Parma, P. 1987, A&AS, 69, 57
Ferrarese, L., Ford, H. C., & Jaffe, W. 1996, ApJ, 470, 444
Floyd, D. J. E., Kukula, M. J., Dunlop, J. S., McLure, R. J., Miller, L., Percival, W. J., Baum, S. A., & O'Dea, C. P. 2004, MNRAS, 355, 196
Floyd, D. J. E., Perlman, E., Leahy, J. P., Beswick, R. J., Jackson, N. J., Sparks, W. B., Axon, D. J., & O'Dea, C. P. 2006a, ApJ, 639, 23
Floyd, D. J. E., et al. 2006b, ApJ, 643, 660
Gebhardt, K., et al. 2000, ApJ, 539, L13
Gopal-Krishna, Dhakulkar, A. R., Wiita, P. J., & Dhurde, S. 2003, A&A, 410, 139
Govoni, F., Falomo, R., Fasano, G., & Scarpa, R. 2000, A&A, 353, 507
Graham, A., Lauer, T. R., Colless, M., & Postman, M. 1996, ApJ, 465, 534
Graham, A. W., Erwin, P., Trujillo, I., & Asensio Ramos, A. 2003, AJ, 125, 2951
Hardcastle, M. J. 1998, MNRAS, 298, 569
Hardcastle, M. J., Worrall, D. M., Birkinshaw, M., Laing, R. A., & Bridle, A. H. 2005, MNRAS, 358, 843
Harvanek, M., & Hardcastle, M. J. 1998, ApJS, 119, 25
Hutchings, J. B., & Neff, S. G. 1992, AJ, 104, 1
Jackson, N., Beswick, R., Pedlar, A., Cole, G. H., Sparks, W. B., Leahy, J. P., Axon, D. J., & Holloway, A. J. 2003, MNRAS, 338, 643
Jackson, N., & Rawlings, S. 1997, MNRAS, 286, 241
Jedrzejewski, R. I. 1987, MNRAS, 226, 747
Jensen, J. B., Tonry, J. L., Thompson, R. I., Ajhar, E. A., Lauer, T. R., Rieke, M. J., Postman, M., & Liu, M. C. 2001, ApJ, 550, 503
Kauffmann, G., & Haehnelt, M. 2000, MNRAS, 311, 576
Khosroshahi, H. G., Wadadekar, Y., & Kembhavi, A. 2000a, ApJ, 533, 162
Khosroshahi, H. G., Wadadekar, Y., Kembhavi, A., & Mobasher, B. 2000b, ApJ, 531, L103
Koekemoer, A. M., Fruchter, A. S., Hook, R. N., & Hack, W. 2002, in *HST* Calibration Workshop: Hubble after the Installation of the ACS and the NICMOS Cooling System, ed. S. Arribas, A. Koekemoer, & B. Whitmore (Baltimore: STScI), 337
Kormendy, J. 1977, ApJ, 218, 333
Krist, J. 1999, TinyTim User Manual (Baltimore: STScI)
Laing, R. A. 1981, MNRAS, 195, 261
Laing, R. A., & Bridle, A. H. 1987, MNRAS, 228, 557
Lara, L., Feretti, L., Giovannini, G., Baum, S., Cotton, W. D., O'Dea, C. P., & Venturi, T. 1999, ApJ, 513, 197
Leahy, J. P., & Perley, R. A. 1991, AJ, 102, 537
Ludke, E., Garrington, S. T., Spencer, R. E., Akujor, C. E., Muxlow, T. W. B., Sanghera, H. S., & Fanti, C. 1998, MNRAS, 299, 467
Madrid, J. P., et al. 2006, ApJS, 164, 307 (Paper I)
Malin, D. F., & Carter, D. 1983, ApJ, 274, 534
Martel, A. R., Sparks, W. B., Allen, M. G., Koekemoer, A. M., & Baum, S. A. 2002, AJ, 123, 1357
Martel, A. R., et al. 1999, ApJS, 122, 81
———. 1998, ApJ, 496, 203
Martini, P., Regan, M. W., Mulchaey, J. S., & Pogge, R. W. 2003, ApJS, 146, 353
McCarthy, P. J., Spinrad, H., & van Breugel, W. 1995, ApJS, 99, 27
McLure, R. J., Kukula, M. J., Dunlop, J. S., Baum, S. A., O'Dea, C. P., & Hughes, D. H. 1999, MNRAS, 308, 377
Merritt, D., & Ferrarese, L. 2001, MNRAS, 320, L30
Miley, G. K., Heckman, T. M., Butcher, H. R., & van Breugel, W. J. M. 1981, ApJ, 247, L5
Miller, J. S., & Sheinis, A. I. 2003, ApJ, 588, L9
Miller, L. 1985, MNRAS, 215, 773
Milvang-Jensen, B., & Jørgensen, I. 1999, Baltic Astron., 8, 535
Morganti, R., Oosterloo, T., Tadhunter, C. N., Aiudi, R., Jones, P., & Villar-Martin, M. 1999, A&AS, 140, 355
Nilsson, K., Heidt, J., Pursimo, T., Sillanpaeae, A., Takalo, L. O., & Jaeger, K. 1997, ApJ, 484, L107
Noll, K. S., et al. 2004, Proc. SPIE, 5487, 281
Padgett, C. A., et al. 2005, BAAS, 37, 1295
Peng, C. Y., Ho, L. C., Impey, C. D., & Rix, H. 2002, AJ, 124, 266
Press, W. H., Teukolsky, S. A., Vetterling, W. T., & Flannery, B. P. 1992, Numerical recipes in FORTAN: The Art of Scientific Computing (2nd ed.; Cambridge: Cambridge Univ. Press)
Quillen, A. C., Bower, G. A., & Stritzinger, M. 2000, ApJS, 128, 85
Ravindranath, S., Ho, L. C., Peng, C. Y., Filippenko, A. V., & Sargent, W. L. W. 2001, AJ, 122, 653
Rawlings, S., Lacy, M., & Eales, S. 1991, MNRAS, 251, 17P
Richstone, D., et al. 1998, Nature, 395, 14
Rothberg, B., & Joseph, R. D. 2004, AJ, 128, 2098
Sadler, E. M., & Gerhard, O. E. 1985, MNRAS, 214, 177
Schlegel, D. J., Finkbeiner, D. P., & Davis, M. 1998, ApJ, 500, 525
Sérsic, J. L. 1968, in Atlas de Galaxes Australes (Cordoba: Obs. Astron.)
Smith, E. P., Heckman, T. M., Bothun, G. D., Romanishin, W., & Balick, B. 1986, ApJ, 306, 64
Smith, H. E., Smith, E. O., & Spinrad, H. 1976, PASP, 88, 621
Spangler, S. R., & Bridle, A. H. 1982, AJ, 87, 1270
Sparks, W. B., & Jorgensen, I. 1993, AJ, 105, 1753
Spencer, R. E., McDowell, J. C., Charlesworth, M., Fanti, C., Parma, P., & Peacock, J. A. 1989, MNRAS, 240, 657

Spinrad, H., Marr, J., Aguilar, L., & Djorgovski, S. 1985, PASP, 97, 932
Springel, V., Di Matteo, T., & Hernquist, L. 2005, ApJ, 620, L79
Strom, R. G., Riley, J. M., Spinrad, H., van Breugel, W. J. M., Djorgovski, S., Liebert, J., & McCarthy, P. J. 1990, A&A, 227, 19
Tadhunter, C., Dickson, R., Morganti, R., Robinson, T. G., Wills, K., Villar-Martin, M., & Hughes, M. 2002, MNRAS, 330, 977
Tadhunter, C. N., Packham, C., Axon, D. J., Jackson, N. J., Hough, J. H., Robinson, A., Young, S., & Sparks, W. 1999, ApJ, 512, L91
Thompson, R. I., & Corbin, M. 1999, Ap&SS, 266, 79
Tilak, A. 2006, Ph.D. thesis, Johns Hopkins Univ.
Tremblay, G. R., Chiaberge, M., Donzelli, C. J., Quillen, A. C., Capetti, A., Sparks, W. B., & Macchetto, F. D. 2007, ApJ, 666, 109
van den Bergh, S. 2000, PASP, 112, 932
van Dokkum, P. G., & Franx, M. 1995, AJ, 110, 2027
Veron-Cetty, M.-P., & Veron, P. 1988, A&A, 204, 28
Wang, J.-M., Chen, Y.-M., & Zhang, F. 2006, ApJ, 647, L17
Wilson, A. S., Young, A. J., & Shopbell, P. L. 2000, ApJ, 544, L27
Zibetti, S., Gavazzi, G., Scodeggio, M., Franzetti, P., & Boselli, A. 2002, ApJ, 579, 261